Anna Carolina Marx Gonçalves

Optical properties of suspended and supported MoS_2 monolayers

Dissertation presented to the Physics Department of the Universidade Federal de Minas Gerais to partially fulfill the Master of Science in Physics degree requirements.

Supervisor: Paulo Sérgio Soares Guimarães

Co-supervisor: Pierre-Louis de Assis

Belo Horizonte

2019

Dados Internacionais de Catalogação na Publicação (CIP)

G636o Gonçalves, Anna Carolina Marx.
Optical properties of suspended and supported MoS2 monolayers / Anna Carolina Marx Gonçalves. – 2019.
55f., enc. : il.

Orientador: Paulo Sérgio Soares Guimarães.
Coorientador: Pierre-Louis de Assis.
Dissertação (mestrado) – Universidade Federal de Minas Gerais, Departamento de Física.
Bibliografia: f. 49-55.

1. Propriedades ópticas. 2. Semicondutores. 3. Matéria condensada. I. Título. II. Guimarães, Paulo Sérgio Soares. III. Assis, Pierre-Louis de. IV. Universidade Federal de Minas Gerais, Departamento de Física.

CDU – 538.9(043)

Elaborada pela Biblioteca Professor Manoel Lopes de Siqueira da UFMG.

Universidade Federal de Minas Gerais
Instituto de Ciências Exatas
Programa de Pós-Graduação em Física
Caixa Postal 702
30.123-970 Belo Horizonte - MG - Brasil

Telefone (xx) (31) 3499 5637
(xx) (31) 3499 5633
Fax (xx) (31) 3499 5688
(xx) (31) 3499 5600
e-mail pgfisica@fisica.ufmg.br

ATA DA SESSÃO DE ARGUIÇÃO DA 628ª DISSERTAÇÃO DO PROGRAMA DE PÓS-GRADUAÇÃO EM FÍSICA DEFENDIDA POR ANNA CAROLINA MARX GONÇALVES, orientada pelo professor Paulo Sérgio Soares Guimarães e coorientada pelo professor Pierre-Louis de Assis para obtenção do grau de **MESTRE EM FÍSICA**. Às 09:00 horas de treze de agosto de 2019, na sala 4123A do Departamento de Física da UFMG, reuniu-se a Comissão Examinadora, composta pelos professores **Paulo Sérgio Soares Guimarães** (Orientador - Departamento de Física/UFMG), **Pierre-Louis de Assis** (Coorientador - Instituto de Física "Gleb Wataghin"/UNICAMP), **Leandro Malard Moreira** (Departamento de Física/UFMG) e pelo doutor **Guilherme Almeida Silva Ribeiro** (Departamento de Física/UFMG) para dar cumprimento ao Artigo 37 do Regimento Geral da UFMG, submetendo a bacharel **ANNA CAROLINA MARX GONÇALVES** à arguição de seu trabalho de dissertação, que recebeu o título de **"Optical properties of suspended and supported MoS2 monolayers"**. Às 14:00 horas do mesmo dia a candidata fez uma exposição oral de seu trabalho durante aproximadamente 50 minutos. Após esta, os membros da comissão prosseguiram com a sua arguição e apresentaram seus pareceres individuais sobre o trabalho, concluindo pela aprovação da candidata.

Belo Horizonte, 13 de agosto de 2019.

Prof. Paulo Sérgio Soares Guimarães
Orientador da estudante
Departamento de Física/UFMG

Prof. Pierre-Louis de Assis
Coorientador da estudante
Instituto de Física/UNICAMP

Prof. Leandro Malard Moreira
Departamento de Física/UFMG

Dr. Guilherme Almeida Silva Ribeiro
Departamento de Física/UFMG

Candidata

Acknowledgements

Esse trabalho é fruto de uma das muitas ideias do meu co-orientador, Pierre, a quem sou imensamente grata. Obrigada por acreditar em mim e confiar que eu seria capaz de entregar este trabalho. Obrigada, também, por todas as discussões, e por se fazer presente no projeto mesmo estando distante.

Ao Paulo, que mais do que meu orientador, é um grande professor, amigo, psicólogo e conselheiro nas horas vagas. Obrigada por absolutamente tudo. Por acreditar que eu seria capaz. Por me escutar quando eu precisava. Por todos os ensinamentos, seja sobre ciência, seja sobre a vida. Por sempre ter uma xícara de café disponível. A minha admiração e gratidão por você são imensas.

Agradeço às grandes mulheres que conheci no laboratório, Bárbara, Ingrid e Juliana. Obrigada por me ensinarem, não somente ciência e práticas de laboratório, mas também a ser mulher, física, numa área cuja maioria são homens. À Juliana, agradeço especialmente por toda colaboração. Esse trabalho não teria sido concluído sem toda sua ajuda. Aos amigos que fiz no laboratório, Rafael, Henrique, Túlio e Thiago, por toda a ajuda e pela amizade que construímos nos últimos anos. Vocês tornaram meus dias melhores, muito obrigada!

Aos amigos que fiz na UFMG, Lucas, Stela, André, Rofolfo, Bel, Bonnie, Rodrigo, obrigada por todas as conversas, risadas e discussões. Vocês tornaram meus dias na federal mais agradáveis. Agradeço especialmente ao Lucas, um grande amigo que fiz nesses últimos sete anos. Obrigada por todos os ensinamentos, conselhos e ajuda. Obrigada pela paciência, pelos desabafos e por sempre estar disponível quando precisei de um ombro e ouvido amigos.

À minha família, principalmente ao meu pai, Claudio, que sempre acreditou no meu potencial e me deu todo apoio para que eu pudesse seguir meus sonhos. Agradeço à família que eu ganhei: avós, tios e sogros. Especialmente à minha sogra, Aline, uma grande amiga que a vida me deu. Também agradeço aos meus amigos do *Povo de Sempre*, especialmente Clara e Chen, por todos esses anos de amizade.

Ao meu namorado, Mateus, obrigada por todos os momentos juntos. Por me incentivar e acreditar em todo meu potencial. Por me ouvir e me aconselhar. Pela paciência e compreensão. Por estar sempre ao meu lado, nos momentos bons e ruins. Eu não teria chegado aqui sem você.

Por fim, agradeço às agências de fomento, Capes, CNPq e Fapemig, cujo apoio financeiro permitiu que este trabalho pudesse ser concluído. Muito obrigada.

Resumo

Dicalcogenetos de metais de transição, como o MoS_2, têm atraído muita atenção na última década, dado que são semicondutores com um gap de energia no infravermelho/visível, abrindo caminho para muitas aplicações tecnológicas e estudos fundamentais. Nesse trabalho, investigamos as propriedades ópticas de monocamadas de MoS_2, tanto suspensas como suportadas em substratos de SiO_2/Si. Espectros de fotoluminescência e Raman foram obtidos em função da temperatura, de 7 K a 300 K, em vácuo. Vemos mudanças significativas no espectro de fotoluminescência das amostras suspensas e suportadas. Além das transições excitônicas características, conhecidas como A e B na literatura, observamos também a emissão de éxcitons carregados (tríons). Apresentamos e explicamos a evolução dessas emissões à medida que varia-se a temperatura. Para baixas temperaturas, duas novas emissões se tornam mais evidentes e as atribuímos a éxcitons ligados a impurezas.

Palavras-chave: Dicalcogenetos de Metais de Transição, MoS_2, monocamada.

Abstract

Transition metal dichalcogenides, like MoS_2, have attracted a lot of attention in the last decade, due to the fact that they are layered semiconductors with an energy gap in the near infrared/visible, opening the way to many technological applications and fundamental studies. In this work we investigate the optical properties of MoS_2 single layers both suspended and supported on a SiO_2/Si substrates. Photoluminescence (PL) and Raman spectra were taken as a function of temperature from 7 K to 300 K in vacuum. We see significant differences in the PL spectra of the suspended and supported samples. In addition to the well-known excitonic features, called A and B in the literature, we observe emission from charged excitons (trions). We show and explain the evolution of these emissions as the temperature changes. At low temperature two new features become more noticeable and we attribute them to bound excitons.

Keywords: Transition Metal Dichalcogenides, MoS_2, monolayer.

List of Figures

List of Tables

Contents

1 Introduction

Transition metal dichalcogenides (TMDs) are a promising family of semiconducting materials for many technological applications [1–9], owning to their intrinsic near infrared/red energy bandgap [10, 11] and the easiness with which these materials can be stacked on top of one another, due to the weak van der Waals interaction between the layers [12]. In addition, their electronic and mechanical properties can be engineered by their surrounding environment, since these two-dimensional materials are highly sensitive to the substrate they are placed on [13].

In the past decade, many studies were done on these materials features and applications, and there is a extensive list of reviews concerning their chemical and physical properties [14–17]. Even though some reports on the optical properties of both suspended and supported TMD monolayers can be found in the literature [18–22], a complete study on the temperature and laser power dependency is lacking. Also, there is not an agreement on characterizing and addressing the features found in the photoluminescence spectra in these studies: bound excitons, associated with defect states, and biexcitons are usually attributed to those unknown states. In this work, we try to identify these features and understand how they differ for the suspended and the supported MoS_2 monolayers. We collect the Raman and photoluminescence spectra in both samples, as a function of temperature and laser power, in vacuum. We see how these features evolve with the change in temperature and propose a model for understanding the nature of these features.

In Chapter 2 we present some of the transition metal dichalcogenides properties, focusing on MoS_2. We briefly describe their electronic band structure, optical and mechanical properties. We also account for the possible substrate effects that can alter the intrinsic features of these thin films and we explain the method we applied in obtaining the monolayers.

Chapter 3 is dedicated to the description of the experimental methods used in this study. We illustrate every step in the production of the substrates, from preparing the wafers for the lithography patterning to the etching process for creating the holes and, finally, the transfer method for placing the monolayers on top of it. We follow with a short description of the Raman and photoluminescence processes, and then we illustrate the experimental setup used in the measurements. The last section is a quick explanation of the AFM method, used in measuring the holes' depth.

The results we obtained are discussed in Chapter 4. We overview the Raman spectra for the supported and suspended monolayers and see that it gives a reasonable confirmation that the films are one-layer thick. We also see indications that the suspended

monolayer might be under stress. The details of the photoluminescence spectra collected are treated separately for the supported and suspended monolayers. We see striking differences between them, and those are addressed individually for each sample.

We conclude our study in Chapter 5, giving a brief summary of this work and address the issues we found throughout the treatment of the photoluminescence spectra. We give possible routes to correct those problems and how we intend to keep our study on the optical properties of the supported and suspended monolayers, not only for MoS_2, but also including another TMD: WS_2.

2 Overview of MoS_2 Features

The family of transition metal dichalcogenides (TMDs) amounts to about 60 different species, with the majority of them being layered structures [23]. The electrical properties of these materials can vary extensively: metallic, semi-metallic, semi-conducting and insulating character can be found in these compounds, according to their atomic coordination in the layer structure.

In this chapter we will review some of the most important features of the semi-conducting layered family MX_2 (M = Mo,W; X = S, Se), focusing specially in MoS_2 properties.

2.1 Layer Structure

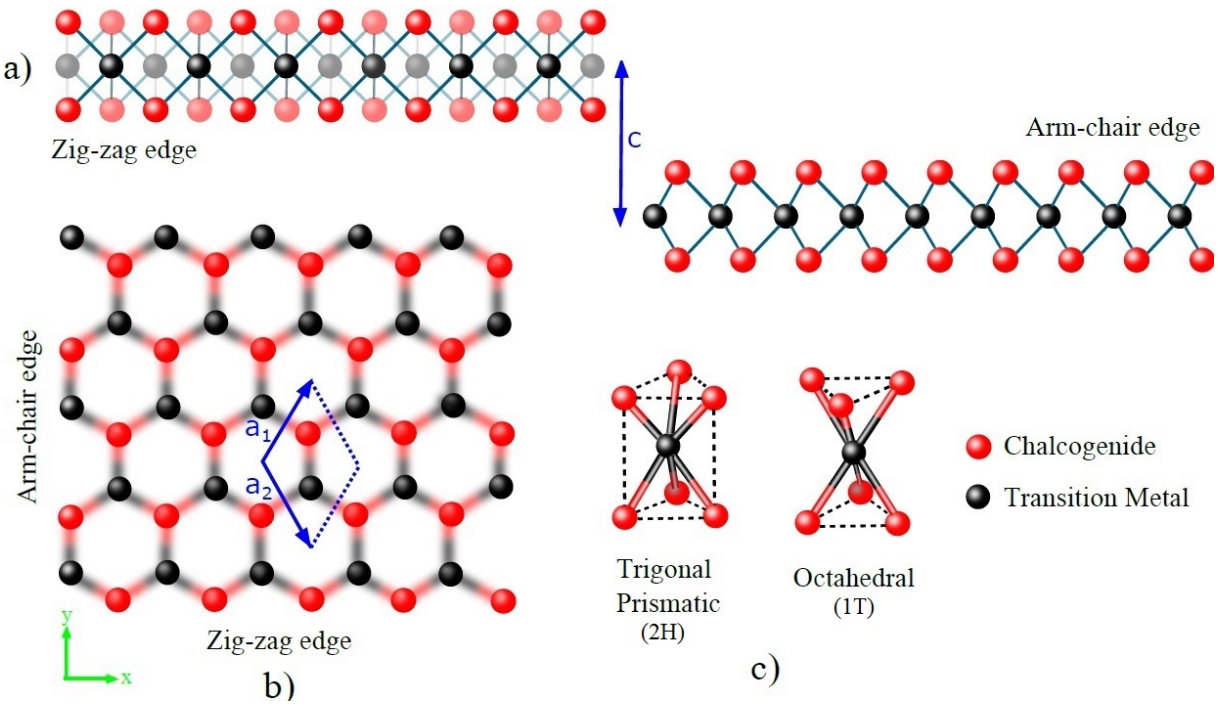

Figure 2.1 – Structure of a prototypical TMD: (a) side and (b) top views of a monolayer; (c) the two atomic arrangements. Extracted from [24].

The structural composition of a monolayer (ML) of semiconducting TMDs is a sandwich-like covalent-bonded layer, where a transition metal sheet is enclosed by two chalcogen planes. In that way, the monolayer can be viewed as tri-layer structure, which is coupled to another identical structure by weak van der Waals interaction. The atoms are arranged in a hexagonal lattice and, depending on their stacking order, these structures

can give rise to many polytypes; the principal ones being in the trigonal prismatic (2H) or octahedral (1T) coordination (see Figure 2.1).

Naturally formed MoS_2 is usually found in the 2H phase, while the 1T arrangement can be obtained via lithium intercalation. In this work, all monolayers are arranged in the 2H phase, since they were obtained from mechanical exfoliation (see Sec. 2.6.1) of MoS_2 crystals.

The 2H phase of bulk TMDs is inversion symmetric, but in the monolayer limit these materials lack an inversion symmetry: taking the molybdenum atom as an inversion centre, the sulfur atoms will be mapped out in an empty space. This gives rise to different behaviours in the band structure and electronic properties of the bulk and monolayer semiconductors[1].

The top view of a TMD structure is that of a honeycomb lattice, similar to graphene, with an inter atomic distance $a = 3.16\,\text{Å}$ and an interlayer separation of $c = 6.41\,\text{Å}$ [23]. This hexagonal Bravais lattice is defined by two lattice vectors, which are related to the lattice parameter a as follows: $\mathbf{a_1} = \frac{a}{2}(1, \sqrt{3})$ and $\mathbf{a_2} = \frac{a}{2}(1, -\sqrt{3})$, drawn in Figure 2.1b.

2.2 Band Structure and Electronic Properties

For a given Bravais lattice there is a corresponding *reciprocal lattice*, defined by a set of wave vectors $\mathbf{k}$ that generate plane waves, $e^{i\mathbf{k}\cdot\mathbf{r}}$, with the same periodicity of the direct lattice [25]. That is, $\mathbf{k}$ is a vector of the reciprocal lattice if

$$e^{i\mathbf{k}\cdot(\mathbf{r}+\mathbf{R})} = e^{i\mathbf{k}\cdot\mathbf{r}}$$

is obeyed for any $\mathbf{r}$, where $\mathbf{R} = n_1\mathbf{a_1} + n_2\mathbf{a_2} + n_3\mathbf{a_3}$[2] (with n_1, n_2 and n_3 being integer numbers) defines the respective Bravais lattice.

The reciprocal lattice can be constructed from primitive vectors $\mathbf{b_i}$ that satisfy

$$\mathbf{b_i} \cdot \mathbf{a_j} = 2\pi\delta_{ij}$$

where $\mathbf{a_j}$ are the primitive vectors of the Bravais lattice and δ_{ij} is the Kronecker delta.

It is possible to define a primitive cell in the reciprocal space that maintains all the symmetry of the lattice. This primitive cell, known as the first Brillouin zone, is a surface enclosing the smallest volume[3] in the space which contains all the information about the lattice and can be translated without overlapping itself. For instance, the primitive vectors of the Brillouin zone for the TMD monolayers, defined in sec. 2.1, generate the

[1] In particular, the emergence of a spin-orbit splitting of the valence band in the ML, which is treated in Sec. 2.2.1.

[2] This is the general case for a three dimensional lattice. In the case of TMD monolayers, we take $\mathbf{a_3} = 0$.

[3] Again, this concerns a general case in three dimensions. The two-dimensional case refers to an area.

reciprocal primitive vectors $\mathbf{b_1} = \frac{2\pi}{a}(1, \frac{1}{\sqrt{3}})$ and $\mathbf{b_2} = \frac{2\pi}{a}(1, -\frac{1}{\sqrt{3}})$, which also describe a hexagonal lattice in the reciprocal space. In Figure 2.2a, the Brillouin zone and respective high symmetry points for these materials are sketched.

The first Brillouin zone plays a major role in the evaluation of a crystal's electronic properties, since the description of the band structure of the material is done in the reciprocal space. An electronic band structure is a set of energy values that an electron, with a defined wave vector within the Brillouin zone, can have. In a simplified way, the electronic energy bands come from the overlapping of the electronic wavefunctions of the N atoms that constitute the crystal. Due to this overlap, each atom's electronic energy levels split into N levels. With so many atoms ($\sim 10^{22}$ cm^{-3}), these levels are so close together that is not possible to resolve them individually, and thus it can be considered a continuum of energies. The range of energies that an electron may have within the crystal is called a *band*, while the set of forbidden values is distinctively called a *gap*.

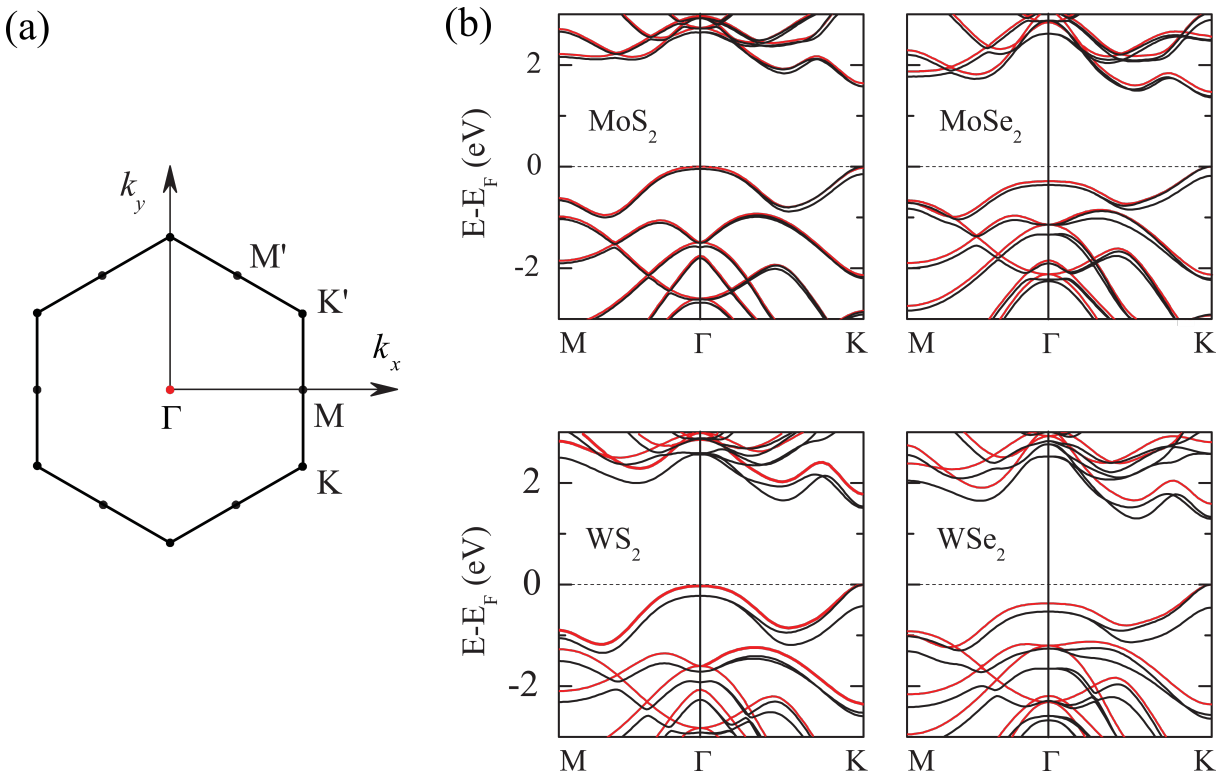

Figure 2.2 – (a) First Brillouin zone of a TMD monolayer with the high symmetry points highlighted: $\Gamma = [0, 0]$, $M = [\frac{1}{2}, 0]$ and $K = [\frac{1}{2}, -\frac{\sqrt{3}}{3}]$. (b) Electronic band structures calculated for some TMD monolayers. M, Γ, K are the high symmetry points as shown in (a) and E_F is the Fermi energy. Black lines include spin-orbit splitting (Sec. 2.2.1) and red lines do not. Adapted from [26].

The electronic band structure can give many informations about the material's electronic properties. The two most important energy bands are the *conduction* and *valence* bands, and their position relative to the Fermi level. The latter is related to the occupation number of electrons in a band, and can be seen as the energy of the most energetic valence

electron in the ground state at zero Kelvin [27]. At room temperature, the Fermi level can be located within a gap or an energy band. For the first situation, the material can be either an insulator or semiconductor, while in the other case, it behaves as a metal.

The highest occupied energy band at zero Kelvin is called the valence band, while the lowest unoccupied energy band at zero Kelvin is known as the conduction band. In metals, these two bands overlap, while in semiconductors and insulators there is a separation between then; for the former the gap is up to 4 eV and can take even greater values in the latter case.

Figure 2.2b shows the band structures calculated for the most studied TMD monolayers. There is a clear bandgap, ocurring at the K point, of approximatelly ~ 2 eV in each material, evidencing their semiconducting behaviour. This bandgap energy value is related to the optical properties of these materials and will be addressed in Section 2.3.

In the complete description of the band structure of a crystalline solid, one needs to account for the properties of all valence electrons by computing the corresponding wavefunction for the system. The exact solution for the Schrödinger equation relies on a set of 3N coupled second order differential equations, where N is the number of electrons in the solid. This task becomes overly complicated to perform computationally, and only approximated solutions are possible.

To deal with this problem, Walter Kohn and John Pople presented a method that relies on the collective properties of the electrons, such as the electron density, to describe the ground state electronic properties of the material: the Density Functional Theory (DFT) [28]. Although this is still the most used method in computing the band structure of many solids, other complementary methods can be used to account for deficiencies in the DFT mode. For example, since DFT has an in-built underestimation of the bandgap value, it cannot account properly for the excited states and its application is limited to lattices with a small number of sites only. The *GW approximation* is a method that uses Green functions to account for the exchange and correlation effects, providing bandgap values closer to the obtained experimental values [29]. Another method is the *tight-binding method*, which is related to the Linear Combination of Atomic Orbitals (LCAO) method and is based upon the linear superposition of atomic wavefunctions in each lattice site [30–32]. There is also the $\mathbf{k} \cdot \mathbf{p}$ *theory*, which relies on a perturbative analysis of the system's Hamiltonian to compute the energy bands [33, 34].

The energy band theory encloses even more information about the electronic features of the crystal. For instance, it is possible to obtain an important parameter based on the curvature of the bands, called the *effective mass*. Taking, as an example, the model of a free-electron, its energy is related to its momentum as

$$E = \frac{p^2}{2m} \tag{2.1}$$

while the momentum p can be written

$$p = \hbar k \tag{2.2}$$

in terms of the wave vector k. Substituting 2.2 into 2.1, we obtain

$$E = \frac{\hbar^2 k^2}{2m} \tag{2.3}$$

which is known as the *energy dispersion relation*. This gives rise to the curvature of the bands in the electronic band structure, since the energy is a function of the square of the wave vector.

The curvature of the bands can be calculated by differentiating the energy twice with respect to the wave number:

$$\frac{\mathrm{d}^2 E}{\mathrm{d}k^2} = \frac{\hbar^2}{m}$$

and conversely we can see that the mass of the electron is an inverse function of the curvature of the bands:

$$m = \frac{\hbar^2}{\mathrm{d}^2 E/\mathrm{d}k^2} \tag{2.4}$$

Although this was calculated for a free-electron model, equation 2.4 still applies to electrons in a crystal, and the generalization would be:

$$m^* = \frac{\hbar^2}{\mathrm{d}^2 E/\mathrm{d}k^2} \tag{2.5}$$

where m^* is called the effective mass of a particle. This becomes an important concept when evaluating the valence and conduction bands, since most commonly they will not have the same curvatures[4].

Not only the curvatures of these bands are generally not the same, but their minima an maxima can be located at different wave numbers. The characteristic energy gap of a material is denoted by the one with with the least energy difference between a conduction band minimum (CBM) and valence band maximum (VBM). If the CBM and VBM are located at different values of k, then the gap is said to be indirect; if they are located at the same k, then the gap is a direct one.

In transition metal dichalcogenides, there is a change from an indirect energy gap to a direct one, when they go from bulk to monolayer [10, 11, 30, 35]. In the monolayer limit, the CBM and VBM are both located at the K point in the Brillouin zone and their separation is of the order of ~ 2 eV, as mentioned before (for MoS_2 the calculated value is 1.9 eV, see Fig. 2.3). Yet, in the bilayer and multi-layer form, the least energetic gap is an indirect one, with the VBM located at the Γ point and the CBM midway between the K and Γ points. This gap is even smaller than the monolayer direct gap, with a value close

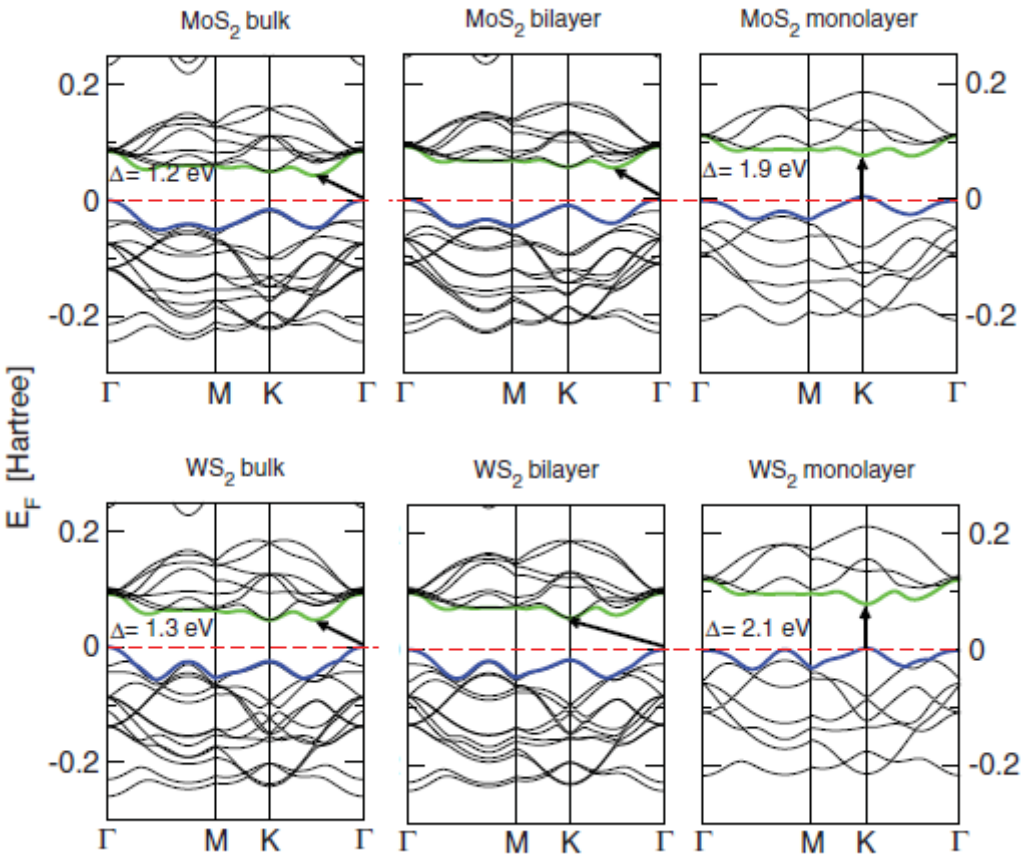

Figure 2.3 – Calculation of the dispersion relation for two different TMDs, MoS_2 (top) and WS_2 (bottom), evidencing the clear transition, as the number of layers is reduced, from an indirect-gap semiconductor in bulk form to a direct-gap one in the monolayer limit. The red dashed line represents the Fermi energy, the green curve is the bottom of the conduction band and the blue line is the top of the valence band. The arrows indicate the fundamental bandgap for each case. Modified from [35].

to 1.2 eV in bulk MoS_2, as shown in Fig 2.3, which also includes the calculated band gaps for mono- and multi-layer WS_2 for comparison.

Some other interesting electronic properties of these TMD monolayers arise due to their reduced size in the direction perpendicular to the layer of atoms and the interaction of the electronic orbitals of the heavy elements in their composition. Those will be accounted for separately in the two sections that follow.

2.2.1 Spin-Orbit Splitting

The electronic configuration of the transition metal atoms shows that the valence electrons are located within the *d*-shell, while for the chalcogenides the electronic distribu-

[4] A brief comment on this is made in Section 2.2.2

tion of the carriers is mainly in the p orbital. In the TMDs, the band structure can be approximated by transition metal's d-orbital partially filled bands between hybridized s-p bands that arise from the transition metal-chalcogen interaction [36].

The valence electrons from the d shell in transition metals exhibit high angular momentum which interacts with the electron's spin magnetic moment, giving rise to a strong spin-orbit coupling (SOC). In this case, the electron spin interacts with the magnetic field created by the electron's orbital angular momentum, thus affecting the energy levels in the band structure. This can be treated by perturbation theory, lifting the energy degeneracy in the band structure in monolayer TMDs and which can be seen as a spin-orbit splitting (SOS) of the valence and conduction bands [26, 36, 37]. Figure 2.2b shows a calculation for the band structure of MoS_2 and WS_2 monolayers including the SOS (black solid lines). It is important to notice that the splitting is much larger in the valence band than it is in the conduction band. This is so, because the valence band is mainly constructed from the d-orbitals, while the conduction band is formed essentially from hybridized s-p orbitals.

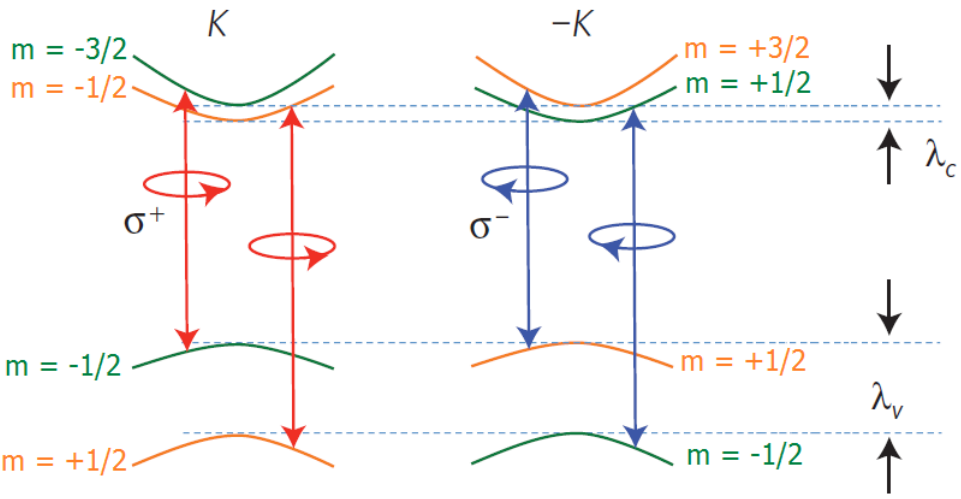

Figure 2.4 – Spin and valley coupling in transition metal dichalcogenides, with the optical selection rules in each valley for a monolayer TMD, evidencing the splitting bands in each point. The SOC induced splitting in the conduction band is denoted by λ_c, while λ_v is the SOC induced splitting in the valence band. The colours represent the spin-locking for each band edge: green for spin-down and orange for spin-up. Adapted from [38].

Another effect on the band structure of these monolayers is due to the lack of inversion symmetry in odd-numbered layers TMDs. In this case, for the lowest energy bands in the high symmetry points, the band edges at K and K' points will have opposite spin signs, which is known as the *spin-valley coupling* [38–40]. In that way, the spin-down state at K is degenerate with the spin-up state at the K' valley, shown schematically in Figure 2.4. This becomes interesting when exciting the electrons from the valence bands

to the conduction bands with polarized light, since the K and K' points will be excited with opposing polarizations, as illustrated in Figure 2.4.

2.2.2 Excitonic Features

An electron in the valence band can be excited to the conduction band provided that it acquires enough energy to cross the energy gap between the bands. When this is the case, the conduction band is filled with an electron and the valence band is left with a deficiency of it. This absence of an electron, called a *hole*, behaves as it was a particle, very similar to the one it was originated from, but has a positive charge and a negative mass associated with it.

The arising positive charge is related to the conservation of charge in the material: since the conduction band has acquired an electron with a negative charge, the crystal must maintain its neutrality and thus the valence band's hole must be positively charged. The negative mass, in turn, comes from the curvature of the top of the valence band, as can be seen from Equation 2.5, which shows that a negative curvature of the band is associated with a negative effective mass.

Both electron and hole are free to move within the crystal's band they are located in and contribute to the crystal's electronic features. Since they have opposite charges, they can interact with each other via Coulomb attraction and this interaction gives rise to a new quasi-particle called the *exciton* [41]. In this view, the excitonic behaviour of a material depends on its energy band structure and also on the dielectric environment it is enclosed.

In a modest approximation, the exciton can be treated within an hydrogenic model, where the negative electron and the positive hole orbit each other. It is possible, then, to characterize them in two different regimes: the Wannier-Mott or Frenkel types. The former describes interactions with a large radius, surrounding many lattice atoms and a small binding energy (see Figure 2.5a); and the latter, in contrast, refers to those with a radius compared to the lattice constant and a strong binding energy (Figure 2.5b).

The formation and stability of excitons in a material depends on their attractive potential, since they can be scattered by other quasi-particles in the material as, for example, phonons[5]. The number of phonons in the system is proportional to the thermal energy, k_BT, where k_B is the Boltzmann constant and T is the temperature. At room temperature, $k_B \sim 0.025\,\text{eV}$. For the Wannier-Mott type of excitons, the large radius imply a small binding energy ($\sim 0.01\,\text{eV}$) and in the Frenkel regime this energy is much higher ($\sim 0.1 - 1\,\text{eV}$). Thus, Wannier-Mott excitons can be seen mainly at cryogenic temperatures, while Frenkel ones are stable at room temperature conditions.

[5] Phonons are quantized vibrational modes of the lattice.

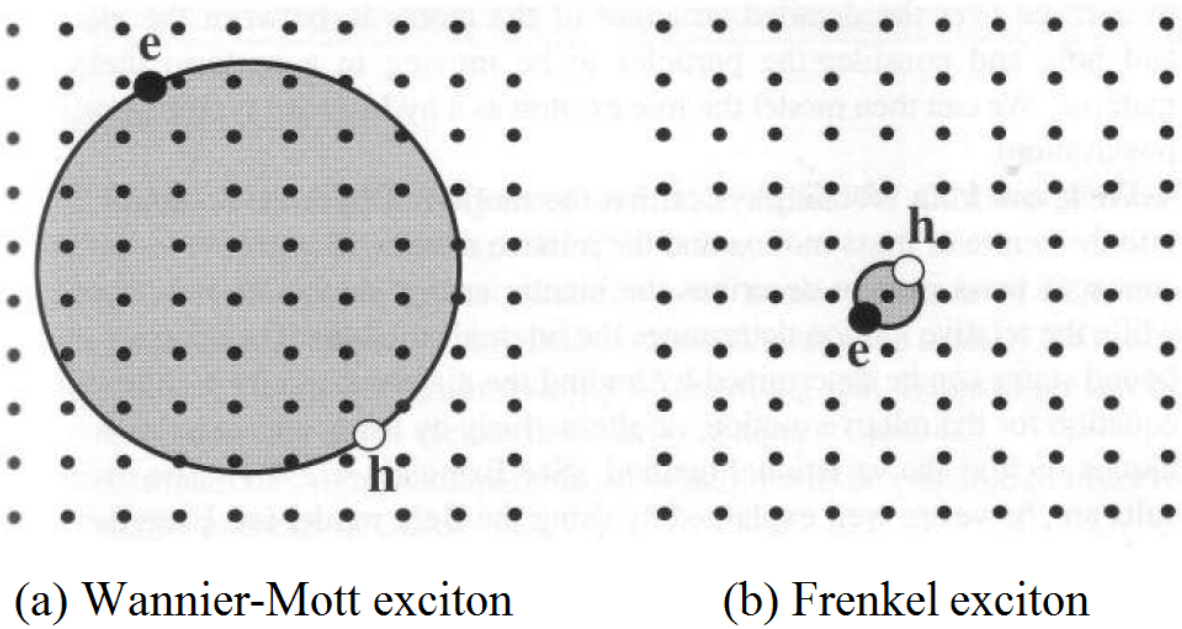

Figure 2.5 – Schematics of the (a) Wannier-Mott and (b) Frenkel excitons. Adapted from [41].

Since TMD monolayers present a strong confinement of electrons in the planar direction, there is a strong excitonic behaviour of these materials even at room temperature [10, 42, 43]. This is characteristic of the Frenkel regime, as the electrons and holes will be spatially close together in the direction perpendicular to the plane of the monolayer. Nonetheless, the excitonic properties in these materials remain mostly close to the Wannier-Mott regime.

Also, the spin-orbit splitting in the valence band, mentioned in Section 2.2.1 gives rise to two excitonic energies, known as excitons A (highest valence band; smallest energy) and B (lowest valence band, highest energy). These excitons are present in all four semiconducting TMDs (MoS_2, WS_2, $MoSe_2$ and WSe_2), with slightly different energies between each other.

Another important excitonic feature of these two-dimensional semiconducting materials are the charged exciton (also known as *trion*) and the system formed in the two-excitons interaction (called *biexciton*). A trion occurs mainly in doped semiconductors, where one of the charge carriers has a higher concentration than the other one. The extra charge carrier interacts with the neutral exciton, forming a charged quasi-particle. A negative trion emerges from the interaction of a neutral exciton and an electron, and a positive trion arises from the hole-exciton state formation. MoS_2 and WS_2 are known to present high negative-trion intensities, in some cases even exceding the neutral-exciton intensity in their luminescence[6] spectrum [44, 45]. In contrast, biexcitons appear in systems with high densities of neutral exciton states and due to the mutual interaction between these

[6] Photoluminescence phenomena is explained in Section 3.2.2.

quasi-particles, the biexciton energy is located below the exciton and trion energies [46–48].

These excitonic features can appear through many mechanisms, such as application of electric fields [44, 49], through high laser excitation powers [45, 47], defect states [48, 50] and doping. The latter is covered in Section 2.5.2 for the substrate-type doping.

2.3 Optical Properties

The light-matter interaction can occur in many different ways. The easiest way to classify them is by accounting the distinct phenomena that can happen, such as reflection, propagation and transmission. As light is shone to the material, some will be reflected from its surface, the remaining light will propagate through the material and whichever (if any) light reaches the back surface of it, it can be either reflected again or transmitted to the other side [41].

When propagating through a medium, there are other optical phenomena that the incident light can experience. Examples are refraction, scattering, absorption, luminescence and non-linear effects, that can change the direction, frequency and intensity of the incoming beam. In refraction, the velocity of the light wave is changed inside the medium and this can lead to the bending of the light rays, described by Snell's law. Scattering is responsible for changing the direction and possibly the frequency of the incident light, and thus reducing the intensity of the collected beam. The absorption process can occur if the frequency of incoming photons is resonant with energetic transitions of the atoms and molecules in the material. The excited atoms can then decay to lower energy states in a radiative or non-radiative way. Radiative processes are associated with a photon's emission, while in non-radiative processes the atom can dissipate energy by other means, such as phonon emission.

These process are important in the characterization and description of the material's optical properties. For instance, refraction and absorption are linked to the complex refractive index $\tilde{n} = n + i\kappa$, where n is a ratio between the velocity of light in two media and κ is the extinction coefficient, which is related to the absorption coefficient (α) as: $\alpha = \frac{4\pi\kappa}{\lambda}$, with λ the wavelength of the light in vacuum [41]. The real part of the refractive index (n) can be used in the optical identification of monolayer TMDs [51], as the optical contrast of these films and the substrate in which they are sitting is related to the difference between their indexes. The absorption coefficient is, in turn, related to the luminescence spectra of these materials, since they will absorb light with frequencies that are at least the size of their bandgap.

The direct gap in the monolayers of the semiconducting transition metal dichalcogenides, along with the spin-orbit splitting and pronounced excitonic behaviour, gives rise to many features in their optical spectra. For instance, their intrinsic bandgap is

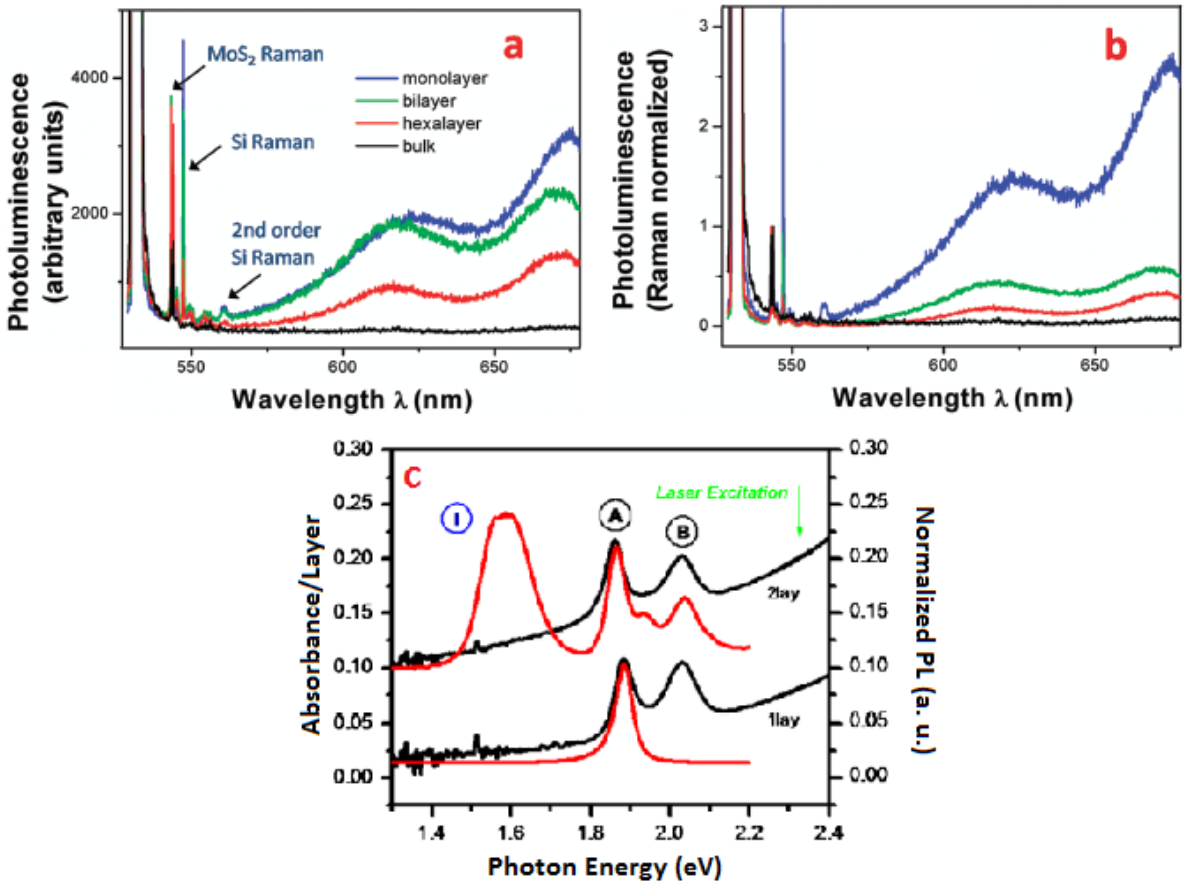

Figure 2.6 – Photoluminescence (PL) spectra of monolayer, bilayer, hexalayer and bulk MoS_2: (a) Original and (b) normalized data. Extracted from [11]. (c) Absorption spectra (black) and corresponding PL (red) from MoS_2 mono and bilayer. A and B are the corresponding excitonic transitions and I is the indirect gap energy. Adapted from [10].

located in the red or infrared part of the electromagnetic spectrum, which accounts for their strong light absorption in the visible region [10]. Not only that, but the direct gap is responsible for the strong luminescence intensity of the monolayers, in contrast with their bulk counterparts, which present an indirect bandgap [11]. These features are shown in Figure 2.6 for MoS_2.

The photoluminescence (PL) spectrum of ML TMDs is characterized by two distinctive peaks, which are attributed to the excitonic transitions at the K (or K') valley, and are labelled A (lowest energy) and B (highest energy). In the case of MoS_2, the experimental values found for these energy transitions are ∼1.8-1.9 eV (A exciton) and ∼2 eV (B exciton).

The PL spectrum is heavily influenced by the temperature. At cryogenic temperatures the excitonic features can be easily resolved from one another and their intensities are usually higher than in room temperature measurements.

2.4 Mechanical Properties

The elastic properties of homogeneous and isotropic materials can be described by the *Young's modulus* (Y), which measures the stiffness of a solid and is defined as:

$$Y = \frac{1}{V_0}\frac{\mathrm{d}^2 E_s}{\mathrm{d}\epsilon^2} \tag{2.6}$$

where ϵ is the strain, E_s is the strain energy (calculated from the difference between the unstrained and strained system) and V_0 is the total volume. For monolayers, instead if calculating the Young's modulus, the *in-plane stiffness*

$$C = \frac{1}{S_0}\frac{\mathrm{d}^2 E_s}{\mathrm{d}\epsilon^2} \tag{2.7}$$

is regarded a better parameter for evaluating the elastic behaviour of the material. In this case, S_0 is the sample's surface area.

Molybdenum disulphide monolayers, although apparent fragile, are regarded as very hard, with in-plane stiffness calculated by Ataca et al. [52] as $\mathrm{C} = 145.8\,\mathrm{N\,m^{-1}}$ and by Yue et al. [53] as $\mathrm{C} = 123\,\mathrm{N\,m^{-1}}$. Also, an experimental value of the Young's modulus was reported to be $\mathrm{Y} = (270 \pm 100)\mathrm{GPa}$, which is comparable to stainless steel (205 GPa) but softer than graphene (1000 GPa) [54].

Another feature of these materials is related to the vibrational modes of the lattice, known as phonons. Phonons are quantized modes of vibration in the material and can be treated as plane waves, where the frequency and wavenumber are related by the dispersion relation. They can be classified as either *optical* or *acoustic*. In the latter case, the motion of the atoms resembles that of an acoustic wave (hence the name), where the displacement of all the constituent atoms will be in the same direction at any given moment. For an optical phonon, the displacement of different charges are in opposite directions. The phonon is called optical because it is usually excited by optical radiation. Figure 2.7 schematically shows the two types of phonons.

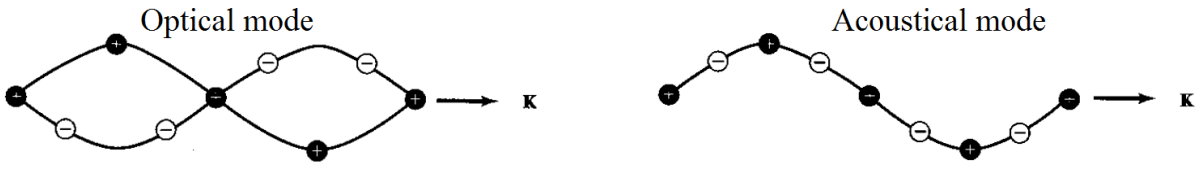

Figure 2.7 – Schematics of the optical and acoustic phonon modes in a diatomic linear lattice. Extracted from [27].

One way to determine at least some of the phonon energies is through Raman spectroscopy, which is explained in Section 3.2.1. The Raman spectrum changes slightly for each type of TMD, but two main frequencies appear consistently in their spectra: the in-plane E^1_{2g} and out-of-plane A_{1g} modes (Figure 2.8). The distance between these two

modes in the Raman spectrum is an indication of the number of layers of the material, as the two modes tend to shift away from each other with increasing thickness [21, 55]. For MoS_2 monolayers, this separation is between 18-19 cm^{-1}.

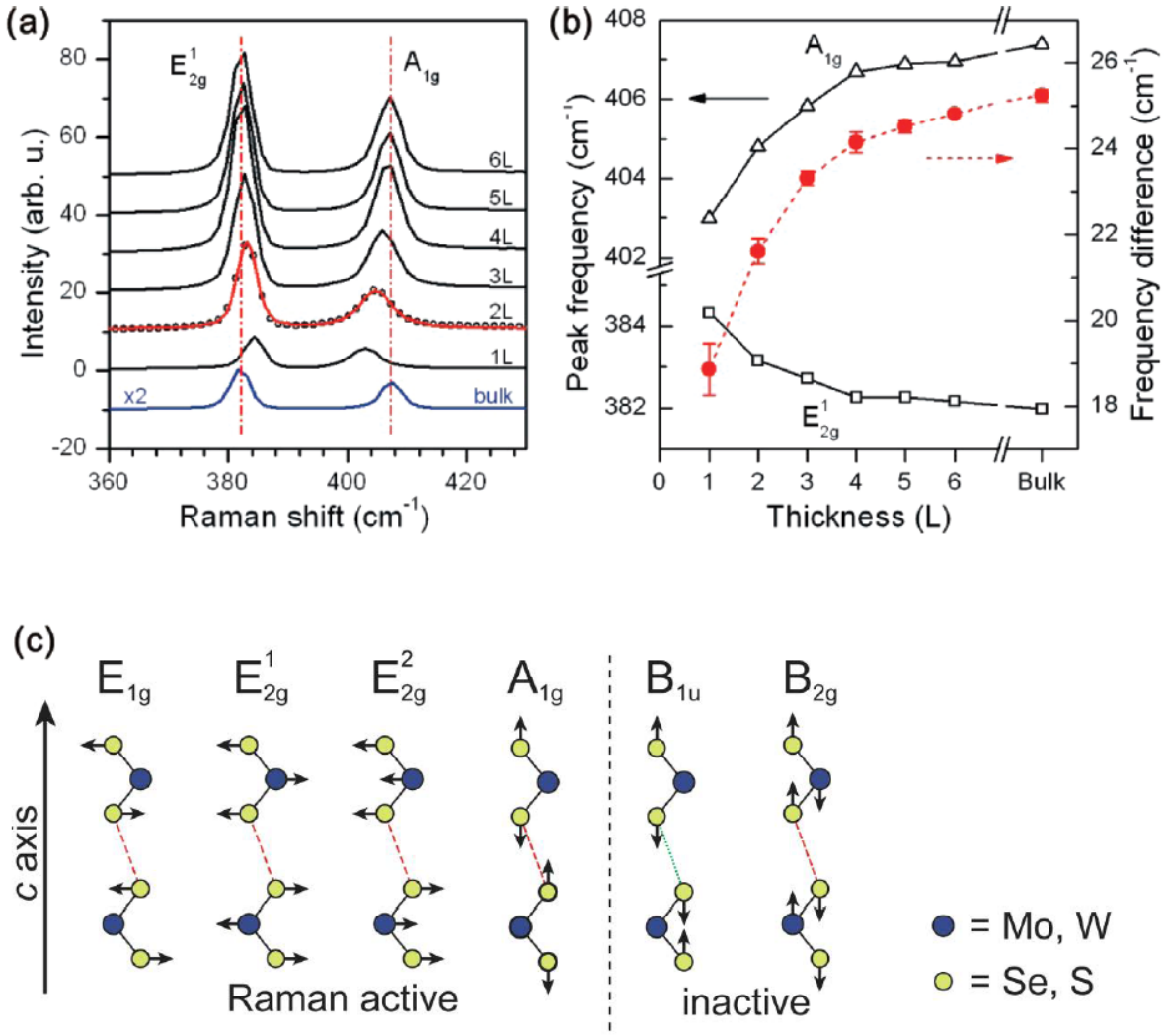

Figure 2.8 – (a) Raman spectra for few- and multilayer MoS_2, evidencing the characteristic frequencies E^1_{2g} and A_{1g}. (b) Dependency with layer tickness for the frequency difference of the main Raman modes of MoS_2. Adapted from [55]. (c) Schematics of the Raman modes for TMDs. Extracted from [50].

2.5 Substrate Effects

The optical and electrical properties of monolayers of transition metal dichalcogenides are heavily influenced by the substrate they sit on, due to the reduced size of the former in the vertical direction. Dielectric constant, defects and charge impurities, roughness and even the thickness of the supporting material can alter the TMDs intrinsic properties.

Since the substrate performs a very important role in the monolayer features, this section is intended to give an insight on how these changes arise. Each point will be briefly covered and the reader is referred to [13] for a detailed account of the substrate influence on TMD monolayers.

2.5.1 Mechanical Strain

There are many different ways to produce strain in two-dimensional materials. As they consist of large-area slabs of reduced thickness, the adherence to a supporting substrate is usually via the van der Waals interaction. Van der Waals forces are proportional to the contact area and, if they are high enough, can deform the monolayers. In the exfoliation process, wrinkles, ripples and even bubbles can appear in these materials; for Chemical Vapour Deposition (CVD)-grown samples, the mismatch between expansion coefficients can cause a strain in the sample during the cooling process [56]. Mechanical strain can also be applied via Atomic Force Microscopy (AFM) indentation [54, 57], engineering of the 2D materials by an elastic polymer substrate [58–62] and suspension over structural arrays [63, 64].

The electronic properties of these materials are known to change with strain application. For instance, the photoluminescence intensity of monolayer MoS_2 is diminished with increasing tensile strain, indicating a cross-over from a direct to an indirect gap [59,63]. Also, a semiconductor to metal transition upon 8% tensile strain and 15% compressive strain was calculated in [65]. Another work related the mechanical coupling of the film with the substrate to the amount of doping in the TMD [18]. In this case, when an MoS_2 film is placed closer and in uniform contact with the substrate, there is an efficient charge transfer to the ML, which appears as an enhanced intensity of the negative trion in the photoluminescence spectrum.

Since the Raman spectra is directly related to the mechanical properties of the material (Sec. 2.4), it will also be affected by the applied strain. A redshift of the active modes, E^1_{2g} and A_{1g}, has been reported for MoS_2 under uniaxial strain [62].

2.5.2 Charge Transfer

In the junction formed between the TMD and the substrate, the charge transfer occurs when electrons flow from the material with the higher Fermi level to that with the lower one. In this process, a surface potential appears, owing to the accumulation of charges in the monolayer, and this can give rise to surface states (such as charge traps). In this way, the electronic structure of the TMDs can be modified, reflecting in changes in the optical and electronic features of the material.

Many works have reported that the photoluminescence emission of a TMD mono-

layer is strongly influenced by the substrate they sit on [18, 66, 67]. There is a noticeable peak shift in the luminescence spectra and the intensity can be enhanced or diminished, depending on the substrate. Not only that, but the luminescence intensity is higher for suspended monolayers, compared to the supported ones [22, 67].

These phenomena are attributed to a charge transfer that occurs between the substrate and the TMDs, suppressing the neutral exciton emission and thus evidencing the emission from the trion.

2.5.3 Optical Interference

The intensity from both Raman and photoluminescence spectroscopy can be either enhanced or reduced by the optical interference arising from reflection and refraction effects at the interface between the monolayer and the substrate. A work done on MoS_2 monolayers, deposited on different types of substrate, shows how this effect takes place [66].

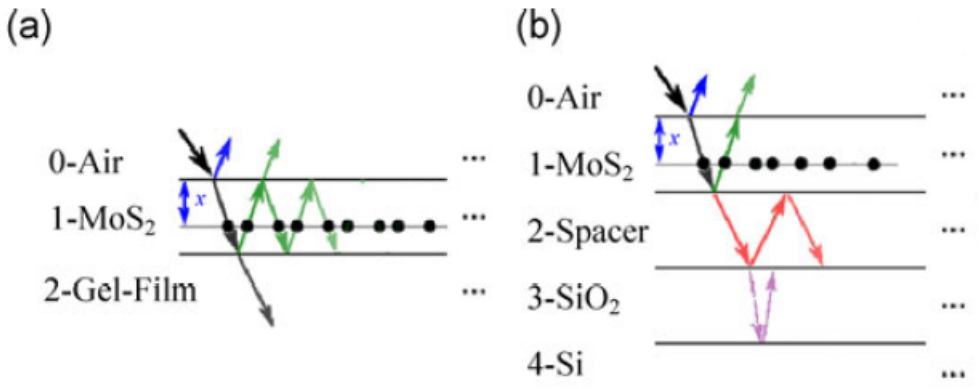

Figure 2.9 – Interference effect on the interface between (a) two and (b) various media, as can be illustrated for the monolayer on top of different substrates. Taken from [66].

The monolayer on top of the substrate is seen as a vertically stacked medium, consisting of three different interfaces: (i) the boundary between the air and the monolayer and (ii) the boundary between the monolayer and the substrate (see Fig. 2.9a). As more layers are added between the interfaces (Fig. 2.9b), the optical path becomes more elaborate. The thickness of each layer, as well as their optical constants, can affect the interference pattern, and thus influence in the resulting intensity.

In the mentioned work [66], it was seen that the intensity of monolayer MoS_2 in different types of substrates can be enhanced by a factor of $\sim$4 compared to that on top of SiO_2.

2.6 Production of Monolayers

There are several ways to obtain few-layer flakes of the TMDs. Top-down approaches include the scotch-tape method (also known as micromechanical cleavage) and chemical exfoliation, while some bottom-up ways are Chemical Vapour Deposition (CVD) [68, 69], Physical Vapour Transport (PVT) and Molecular-Beam Epitaxy (MBE) [70]. Samples obtained in top-down approaches have a higher quality and are suitable for studying the intrinsic characteristics of the material. On the other hand, bottom-up methods produce larger flakes, which is desirable for application in electronic and optical devices, but the samples generally have a large amount of impurities and consequently a lower quality compared to the ones produced via top-down approaches.

For the purpose of our work we used the mechanical exfoliation technique to obtain the monolayers, as we wanted few μm large sheets and the least amount of defects as possible.

2.6.1 Mechanical Exfoliation

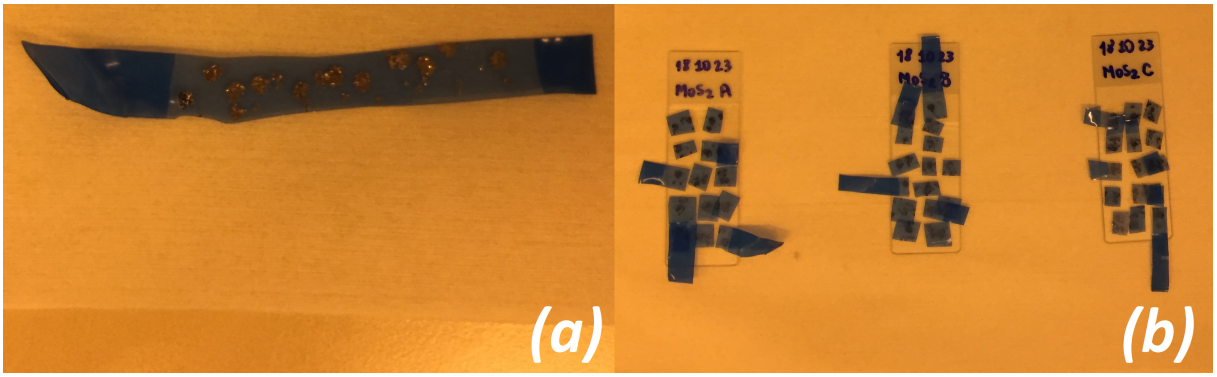

Figure 2.10 – Mechanical exfoliation process. The yellowness of the picture comes from the clean-room's illumination, place where the samples were produced. (a) Tape covered with flakes of MoS_2. (b) Flakes of MoS_2 being transfered to a viscoelastic material (gel film).

The layered structure of these TMDs makes it possible to obtain few layer samples by mechanically exfoliating the crystals, in a technique known as micromechanical cleavage, first used in the production of graphene [71, 72]. In the process, a tiny piece of the crystal is placed on an adhesive tape and from it small flakes of the material will be originated, reason why this first piece of bulk crystal is commonly called *seed*. Another tape is pressed against the one containing the seed, and a few flakes are transferred to this strip. These are generally multi-layer flakes, and the few and single layer ones are often not as many. To overcome this issue and facilitate finding fewer layer regions, this new tape is pressed against itself and to other tapes if necessary, exfoliating the multi-layer flakes. An image of a tape made in this process is shown in Figure 2.10a.

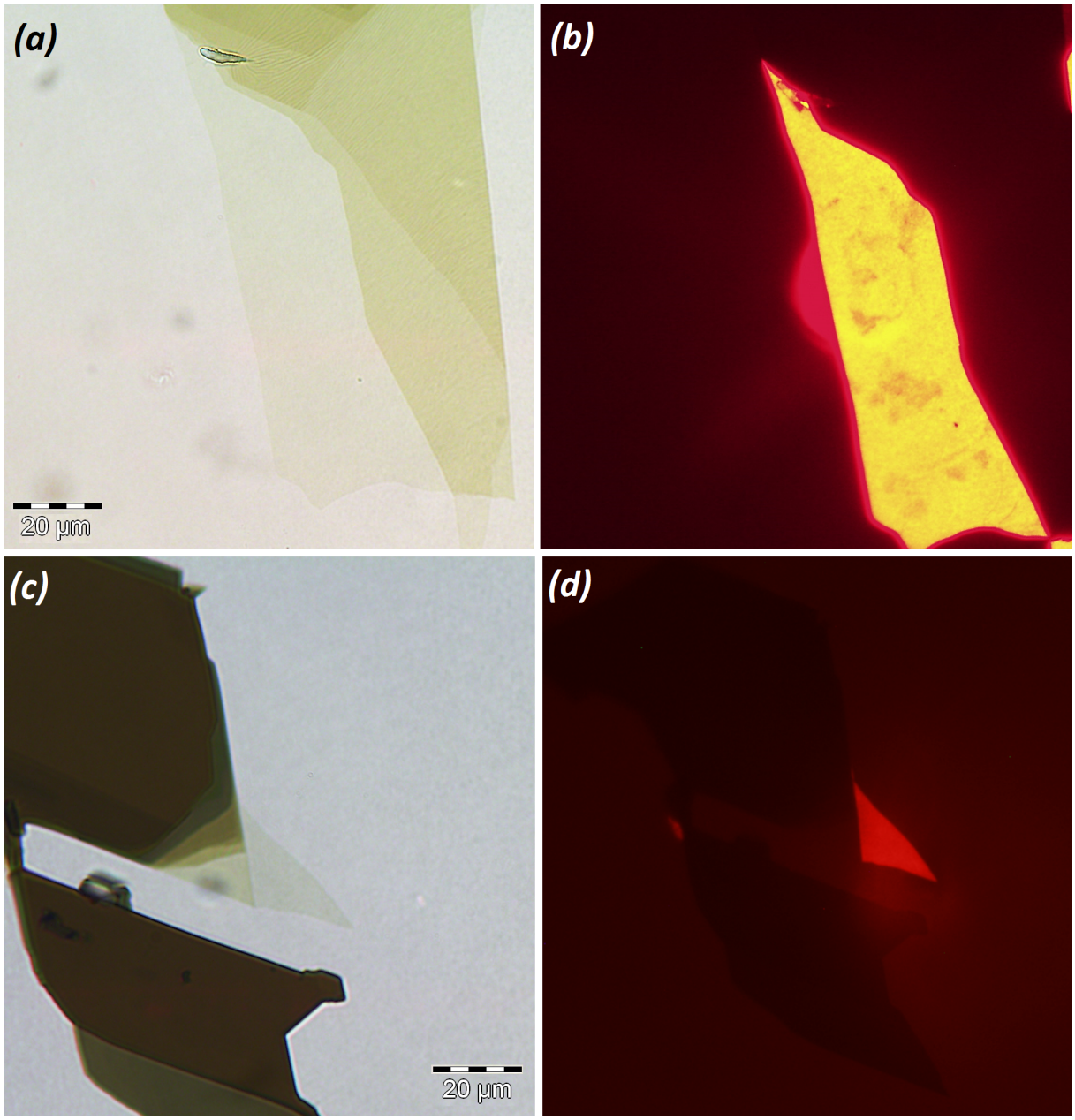

Figure 2.11 – Exfoliated monolayers of TMDs characterized by (a, c) optical and (b, d) fluorescence microscopy. Top is WS_2 and bottom is MoS_2.

After filling the tape with flakes, a last exfoliation is necessary to transfer them to a desired substrate (commonly a SiO_2/Si wafer or a transparent gelfilm). The tape is cut into pieces, carefully enclosing one or two flakes, and then each piece is put in contact with the supporting material, as demonstrated in Figure 2.10b. Each slice of tape is slowly peeled off from the substrate, leaving as many flakes as possible on the latter. The prepared samples are then taken to an optical microscope, where the *mapping* process takes place. In this step, optical contrast between the flakes and the supporting substrate is used to identify prospective monolayers. Since one-layer TMDs are direct gap semiconductors (Sec. 2.2) and bilayers to bulk are indirect ones, the probable candidates from the last step are

confirmed (or discarded) using fluorescence microscopy. This imaging technique relies on the radiation emitted by the sample, when excited by an ultraviolet (mercury) lamp, so monolayers will appear brighter than all the rest. Figure 2.11 shows examples of exfoliated monolayers found by optical and fluorescence microscopy.

3 Experimental Methods

The goal of this project was to observe and understand the changes in the optical features of strained monolayers of MoS_2. To accomplish that, we performed Raman and photoluminescence spectroscopies in MoS_2 monolayers, suspended over pre-etched holes in a SiO_2/Si substrate, to try and understand the differences in both suspended and substrate-supported monolayers. The procedures employed in making the sample, as well as the experimental setup used to measure them, are described in the sections below.

3.1 Sample Preparation

To create the holes in the substrate, we used electron-beam lithography followed by fluorine-buffered etching.

The process of lithography consists in exposing a sensitive film, known as resist, to a beam of either light (photolithography or optical lithography) or electrons (electron-beam or e-beam lithography) in order to draw patterns on the surface of the resist. The exposed material is then treated in a developer solution, dissolving part of the resistive film. There are two types of resist: positive and negative ones. For positive resist, the surface exposed is dissolved in the development process, while for negative resist, the developer acts on the unexposed surface.

For the photolithography process, the pattern resolution is limited by the optical apparatus and the wavelength of the light (generally UV) to about 1 µm, while in electron-beam lithography this resolution can be sized-down to write sub-nm features. For the purpose of this work, the holes were designed to have about 5 µm in size and e-beam lithography was used for better hole definition in the matrices.

We prepared the substrates by spin-coating them with a positive resist film (PMMA 950K-C4). Each wafer was covered with a few drops of PMMA and put to rotate for 1 minute in a spinner. To form a thin even coat of resist in the surface of the substrate, the rotation velocity of the spinner was set to 4000 rpm and the centripetal acceleration to 500 rpm/s. Next, the wafer was heated by 180 °C for 90 seconds in a hot plate, to solidify the resist film and evaporate solvents at the interface.

The following step was drawing the desired pattern in the substrate via e-beam lithography. To achieve the intended size and definition of the hole shape, the parameters set for the incident electronic beam were an acceleration tension of 20 kV and a 225 µC cm^{-2} dose. We wanted to explore different shapes of cavities to study how the strain would affect the clamping parameters, so we designed three types of matrices: circles, squares

and equilateral triangles (see Fig. 3.1).

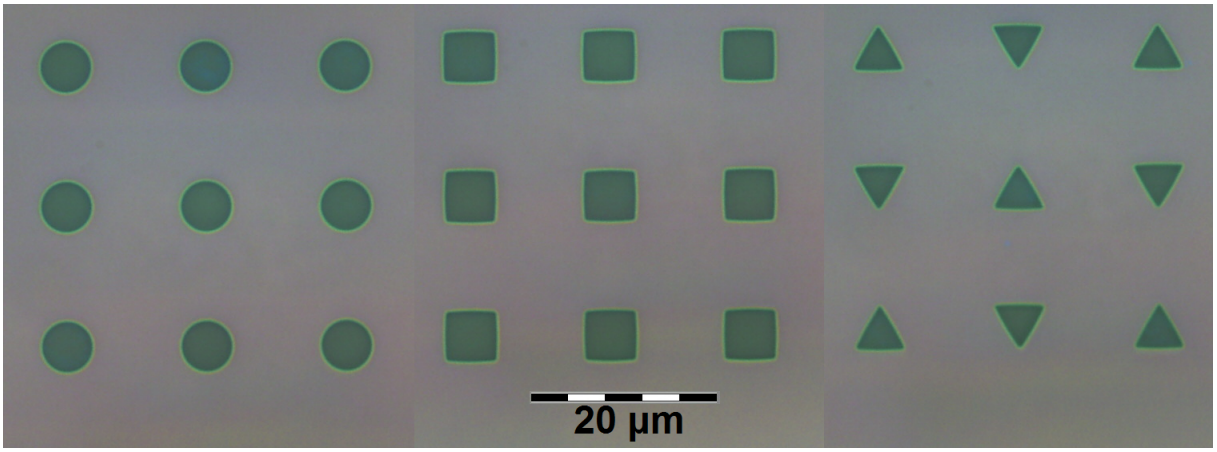

Figure 3.1 – The three types of shapes drawn via lithography, after etching the substrate. Circles have 5 µm diameter, and squares and triangles have sides of 5 µm in size. Each shape centre is spaced by about 15 µm from the adjacent one.

After writing on the resist-covered-substrates, they were immersed in a ∼3 mL developer solution consisting of isopropyl alcohool (IPA) and methyl isobutyl ketone (MIBK) in a 3:1 proportion. Each substrate was left for about 2 minutes in the solution, washed out with IPA for about 30 seconds and dried out with compressed air. In this step, the exposed resist is removed by the developer, leaving a mask of unexposed resist over the wafer surface. This mask permits the surface that is not covered to be removed by an etching mechanism.

To remove the exposed SiO_2 layer, we used a fluorine-buffered etching, prepared from 28 mL of hydrogen fluoride (HF), 170 mL of deionized water (DI H_2O) and 113 g of ammonium fluoride (NH_4F). The substrates were left in the solution for 4 minutes and 30 seconds, then washed out with DI H_2O for a short time and left to dry (some of them were dried with compressed air, resulting in no difference from the other ones). The rate of etching with this recipe in SiO_2 is approximately 70 nm/min, which would result in holes with ∼300 nm depth (the SiO_2 layer is about 285 nm, which means that some of the Si layer would be removed as well). From previous try-outs we saw that this rate is not linear in time, and the holes created were not as deep, as evidenced by AFM measurements (see Sec. 3.3).

After etching the substrate, the PMMA needed to be removed. Two processes were used in this step. First, the substrates were immersed in a 60 °C heated acetone in a hot plate for about 5 minutes, then cleaned with IPA and dried out with compressed air. The second method was a plasma-cleaning session. The wafers were left in a plasma chamber filled with O_2 gas, with a pressure of 0.300 mTorr, for about 20 minutes. The first 10 minutes were used to purge the chamber and in the remaining 10 minutes, a RF power of 150 W was turned on, so ionized gas particles would gain enough kinetic energy to clean

the samples and get rid of the remaining PMMA. Some of the etched, cleaned substrate matrices are shown in Figure 3.1.

The final step was the transfer of MoS_2 monolayers to the pre-etched wafers. We adapted the system used in Ref. [73] and also depicted in Fig. 3.2a, but instead of a microscope, a long-working distance objective was attached to a camera connected to a screen. The method used for transferring the monolayers to the substrate is also based on this same reference.

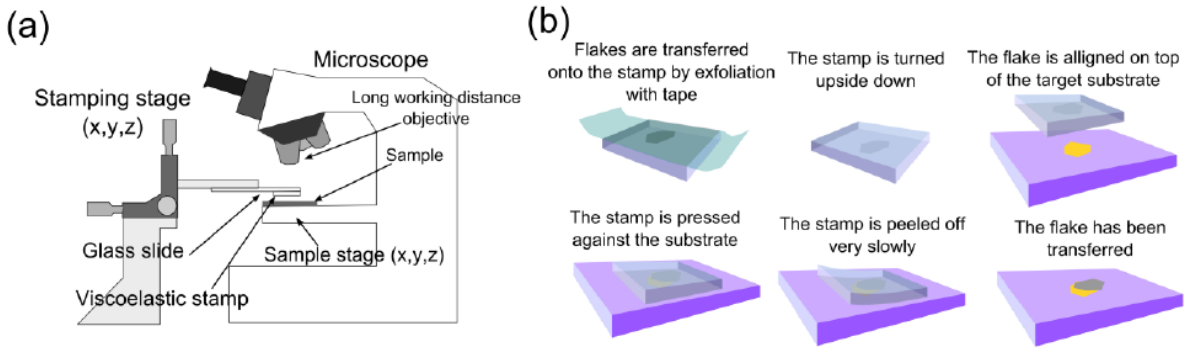

Figure 3.2 – Schematics of the transference (a) system and (b) method used in suspending the MoS_2 monolayers over the hole matrices in SiO_2 substrates. Extracted from [73].

A brief description of the transfer method is depicted in Figure 3.2b. Firstly, MoS_2 (crystal from HQ-Graphene) flakes are transferred to a small piece of a viscoelastic material (a Gelfilm from Gelpak) by the exfoliation technique and the monolayers are identified in the same way described in Sec. 2.6.1. The substrate is then fixed to the sample stage and the film containing the selected monolayer is put on a glass slide, which is turned upside down and placed above the substrate. Since the film is transparent, it is possible to align the monolayer on the wafer surface, in a way that it lays just above the holes in the patterned matrix.

The monolayer is brought near the surface of the wafer and the substrate is heated to 50-60 °C. By slowly pressing the film over the substrate for about 2 minutes and then slowly peeling it off, the monolayer is adhered to the SiO_2 surface, covering the etched holes. This last step was the one most prone to failures and a lot of try outs were needed before achieving satisfactory results. Figure 3.3 shows two samples obtained using this technique.

Since the optical properties of these materials are affected by the substrate (see Section 2.5), the free-standing monolayers should present stronger luminescence than the substrate-supported ones. This was used as an indication that the transfer method was successful and the monolayers were actually suspended over the holes. To observe that, we performed fluorescence microscopy in the final samples, and observed that in fact the

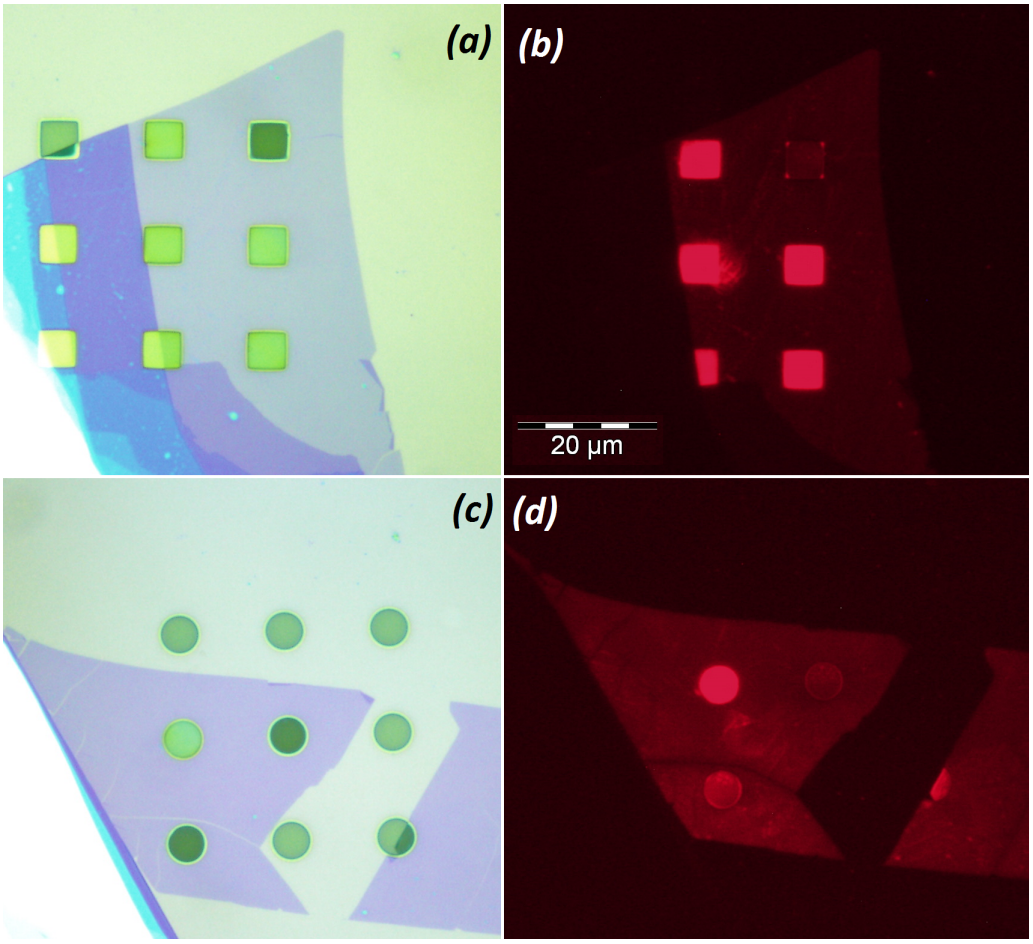

Figure 3.3 – Samples of MoS_2 over different hole shapes in SiO_2 obtained by the methods described in this section. (a) Optical microscopy and (b) fluorescence microscopy images of MoS_2 suspended over squared holes. (c) Optical microscopy and (d) fluorescence microscopy images of MoS_2 suspended over a circular hole.

suspended monolayers had a higher emission yield than the supported ones (Fig. 3.3).

In Figure 3.3, the light-purple area enclosing some of the holes in (a,b) are the MoS_2 monolayers, while few-layer ones are the darker-purple/blue regions. The light-green squares and circle are the covered holes where the monolayer is suspended, while the darker-green ones represent the region where the monolayer collapsed to the bottom of the hole. The suspended monolayers are the brightest features in Figure 3.3(b,d), while the supported and collapsed ones can still be seen, but not as bright.

Finally, we wanted to apply strain to these samples and perform optical measurements to observe the changes in the monolayer. To do so, we used the fact that TMDs are impermeable to standard gases, so the covered hole could be seen as a cavity with trapped air molecules and pressure equal to the atmospheric pressure. Placing this sample in vacuum would create a pressure difference between the inside and outside of the cavity, making the monolayer bulge [63, 74], and consequently causing a tensile strain in it, as

shown schematically in Figure 3.4.

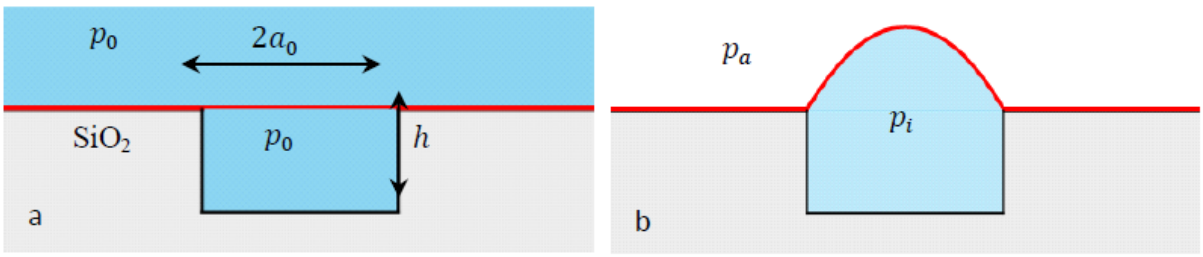

Figure 3.4 – Schematics for creating a tensile strain in the suspended MoS_2 monolayers by putting the sample in a vacuum chamber. p_0 is the atmospheric pressure, p_a is the vacuum pressure and p_i is the pressure inside the cavity when the system is put on vacuum. h is the height of the hole and $2a_0$ is the lateral size (for squares and triangles, for circles is the diameter). Adapted from [74].

3.2 Raman and Photoluminescence Spectroscopy

As incident light can be reflected, absorbed or transmitted by a material, the light-matter interaction can result in a plethora of phenomena. Studying these interactions and related phenomena, it is possible to obtain information about many physical properties of the corresponding material.

3.2.1 Raman Spectroscopy

Raman spectroscopy is an experimental technique that uses the inelastic scattering of light to give information about the vibrational properties of the material. The method consists of shining a monochromatic beam of light through the sample and collecting the scattered light from it. In the elastic scattering, known as Rayleigh scattering, the light collected has the same frequency as the incident light, while in the inelastic scattering, or Raman scattering, the incoming and outgoing light have slightly different frequencies.

When interacting with the material, the incident photons exchange energy with it. If during the interaction the incident photon loses energy to the lattice, the frequency of the collected light will be lower than the incoming one, which is associated with the Stokes process. When the the out-coming light is higher in frequency than the incoming one, meaning that the incident photon gained energy from the lattice, it is said to be a anti-Stokes process. These exchanges in energy between the photon and the lattice are related to the creation and annihilation of phonons in the material, which are quasi-particles associated with the vibrational modes in the lattice. These interactions are sketched in Figure 4.2.

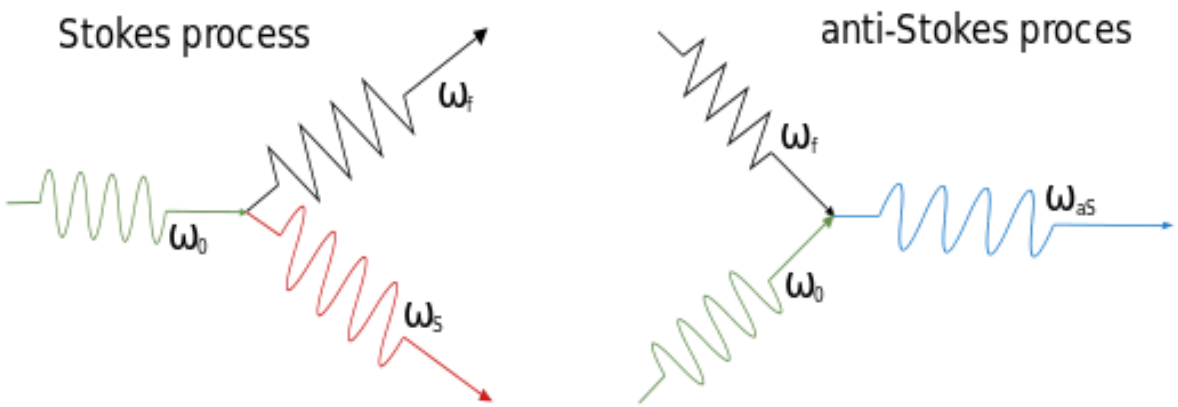

Figure 3.5 – Diagrams for the Stokes and anti-Stokes processes associated with Raman scattering. ω_f is the phonon frequency, ω_0 is the absorbed photon frequency, ω_S and ω_{aS} are the emitted photon frequencies for the Stokes and anti-Stokes process, respectively.

Since the frequency distance between the modes A_{1g} and E^1_{2g} can be an indication of the number of layers in MoS_2 flakes (Sec. 2.3), Raman spectroscopy was used to assure that the flake transferred to the sample was in fact a monolayer.

3.2.2 Photoluminescence Spectroscopy

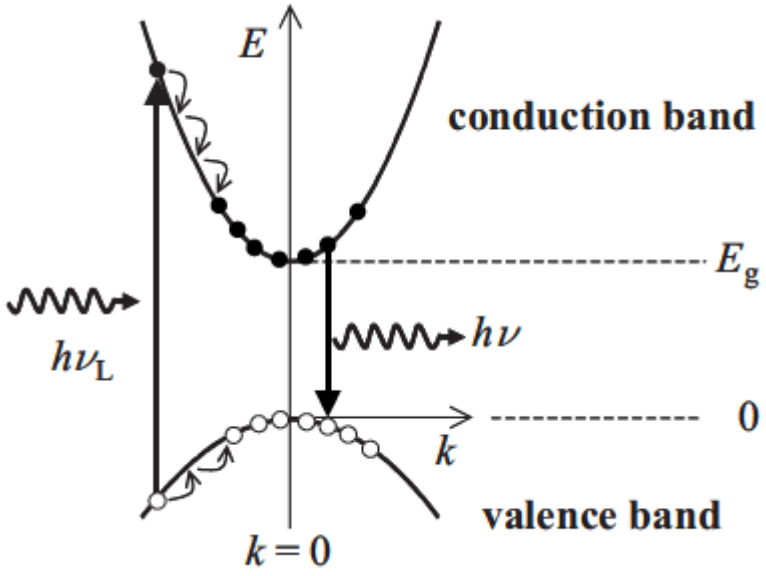

Figure 3.6 – Diagram for the photoluminescence process in a direct-gap material. Adapted from [41].

The process in which the material emits electromagnetic radiation through an electron decay from a higher energy level to a lower energy level is called luminescence. In solids, this process usually arises from the transitions between the conduction and valence

bands. When the material re-emits radiation after absorbing photons with higher energy than the emitted ones, the process is called photoluminescence (PL).

For materials with a direct gap, as is the case of MoS_2 monolayers, the absorbed photon promotes and electron from the valence band to a higher energy state in the conduction band, leaving a hole in the valence band. The energetic state in which the promoted electron is sent to depends on the energy of the incoming photon. This electron quickly decays to the bottom of the conduction band by means of non-radiative processes (i.e. creating phonons). This is so, because these non-radiative processes occur in a shorter ($\sim 10^{-13}$ s) time-scale than for the radiative one ($\sim 10^{-9}$ s). After reaching the bottom of the conduction band, the electron re-combines with the hole it left in the valence band, emitting a photon with energy equal to the gap of the material (Figure 3.6). In the case of the MoS_2, the emitted photon energy corresponds to the excitonic transitions in the material, as discussed in Sec. 2.2.2.

3.2.3 Experimental Setup

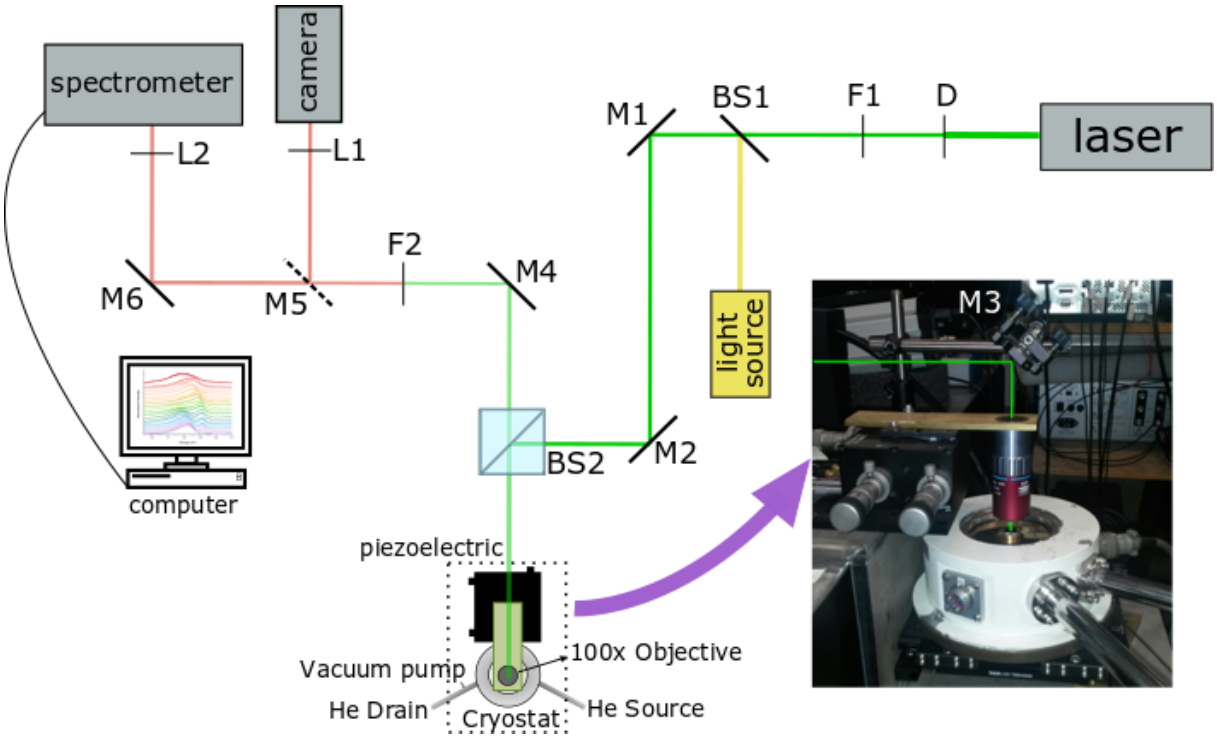

Figure 3.7 – Experimental setup for Raman and PL measurements in our laboratory. Adapted from [24].

The experimental setup used in photoluminescence as well as Raman spectroscopy measurements is shown in Figure 3.7. The sample is placed in a cryostat, which is vertically aligned with the objective (in a different plane of that indicated in the figure, see inset). To direct the laser beam to the sample, a mirror (M3) is placed above the objective (see

inset). A light source and a camera were used to identify the location within the sample where the spectra would be taken.

An incident laser of 568 nm follows the path illustrated in the figure. A diaphragm (D) and an intensity filter (F1) are used to control the intensity of the incoming laser. Two mirrors (M1 and M2) redirect the beam to a 90:10 beam-splitter (BS2), which divides the beam in two. The one with lower intensity is sent in the cryostat direction, passing through a 100x magnification objective attached to an electronic controlled piezoelectric station. The light emitted by the sample is collected by the same objective, passes through the beam-splitter BS2, with 90% of it being transmitted, is deflected by another mirror (M4) and then passes through a high-pass filter (F2) of 568 nm, to suppress the reflected laser line. This is needed as we want to observe the signal coming from the sample only. Another mirror (M6) is used to redirect the beam to the spectrometer and a mobile mirror (M5) is placed between F2 and M6 to redirect the laser to a camera, when one wants to see the actual optical image of the sample. Two 100 mm convergent lenses (L1 and L2) are used to focus the beam to either sensor.

In spectroscopy measurements, a light source excites the sample, which in return produces a response signal. This signal is sent to a monochromator, consisting (roughly) of diffraction grattings that select an interval of wavelengths that are detected by a charge coupled device (CCD). In our measurements, we used a Horiba iHR-550 spectrometer with both 600 lines/mm (photoluminescence measurements) and 1200 lines/mm (Raman) gratings coupled to a Horiba Synphony II CCD device.

We performed low-temperature measurements, placing the sample in a cryostat and cooling it with liquid Helium. To produce vacuum, an Edwards XDS10 pumping station was used, lowering the pressure inside the cryostat to $\sim 10^{-5}$ Pa, before opening the He source to cool down the sample. For the Raman measurements, a laser power of 1 mW was used, while for photoluminescence measurements, we used 4 different values (400, 600, 800 and 1000 µW), in order to observe possible energy shifts and changes in peak intensities.

3.3 Atomic Force Microscopy

Atomic Force Microscopy (AFM) is an experimental technique that gives information about the material's morphology by scanning its surface with a small probe. This scanning probe method was developed by Binnig [75] from his Scanning Tunneling Microscopy (STM) technique. The AFM measurement is based on the displacement of the scanning probe, caused by attractive or repulsive forces between the probe's tip and the atoms on the surface of the material being scanned.

In a short description, a cantilever is attached to piezoelectric material that is carried by a support. At the free end of the cantilever, there is a small sharp tip acting

as a scanning probe. In that way, the tip is put in contact with the sample's surface and its motion on the sample is controlled by the piezoelectric. A laser beam impinges at the end of the cantilever and the reflected light is collected by a detector, which is sensitive to changes in the collected signal. When the tip is displaced vertically, the collected signal changes, as the light reflected by the end of the cantilever is shifted. The piezoelectric responds to this change by acting on the cantilever, maintaining constant the distance between the surface and the tip. Figure 3.8 shows the schematical configuration of an atomic force miscroscope.

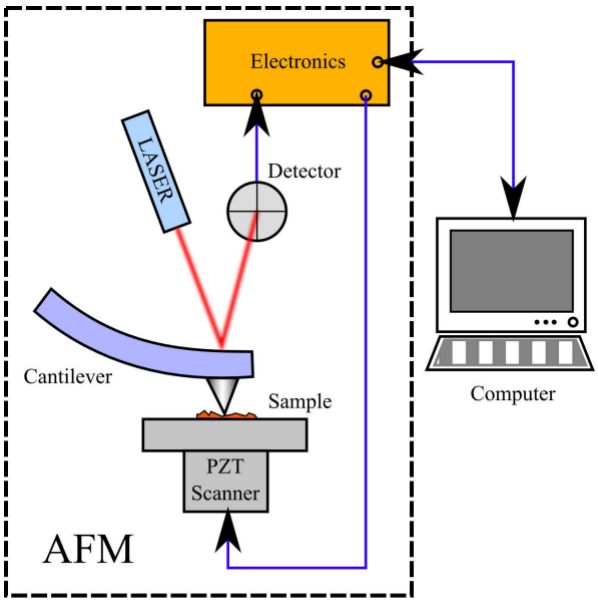

Figure 3.8 – Schematical configuration of an atomic force microscope. Extracted from [57].

In this work, the AFM was used to measure the depth of the etched holes. Figure 3.9 shows the AFM image and height profile of square holes made on SiO_2/Si substrate. From the height profile, we extracted a value of approximately 190 nm for the holes depth.

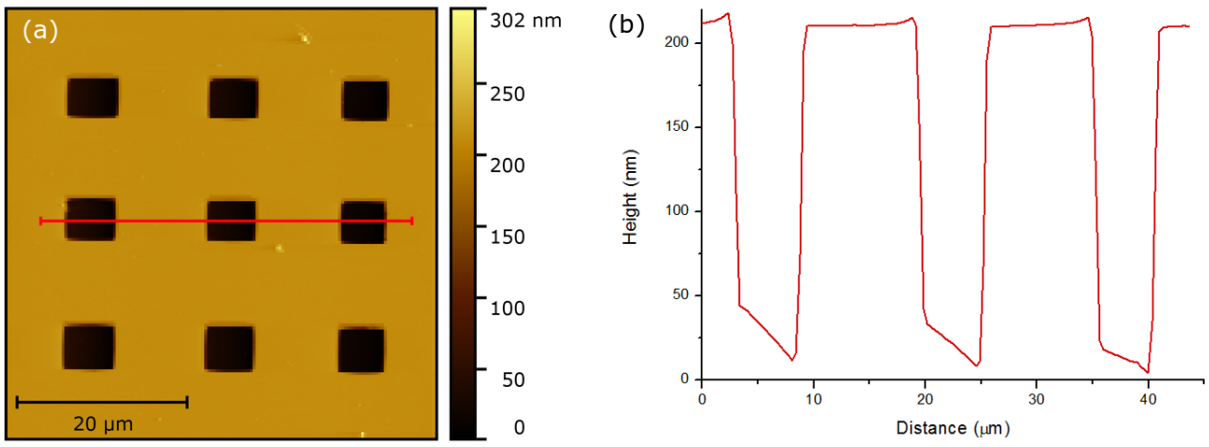

Figure 3.9 – AFM (a) image and (b) profile of the square hole matrix.

4 Results and Discussion

In this work we collected both Raman and photoluminescence (PL) spectra of four different suspended points and three supported ones of a MoS_2 monolayer. All measurements were carried out in vacuum and at different temperatures, ranging from 7 K to 300 K. The points measured are shown in Figure 4.1a. Figure 4.1b shows the fluorescence image of the sample, indicating that the suspended monolayers are brighter than the supported ones. The right-most square (next to point 2 and above point 5) is not as bright as the suspended ones because the monolayer has collapsed to the bottom of the hole. This case is not of interest for this study.

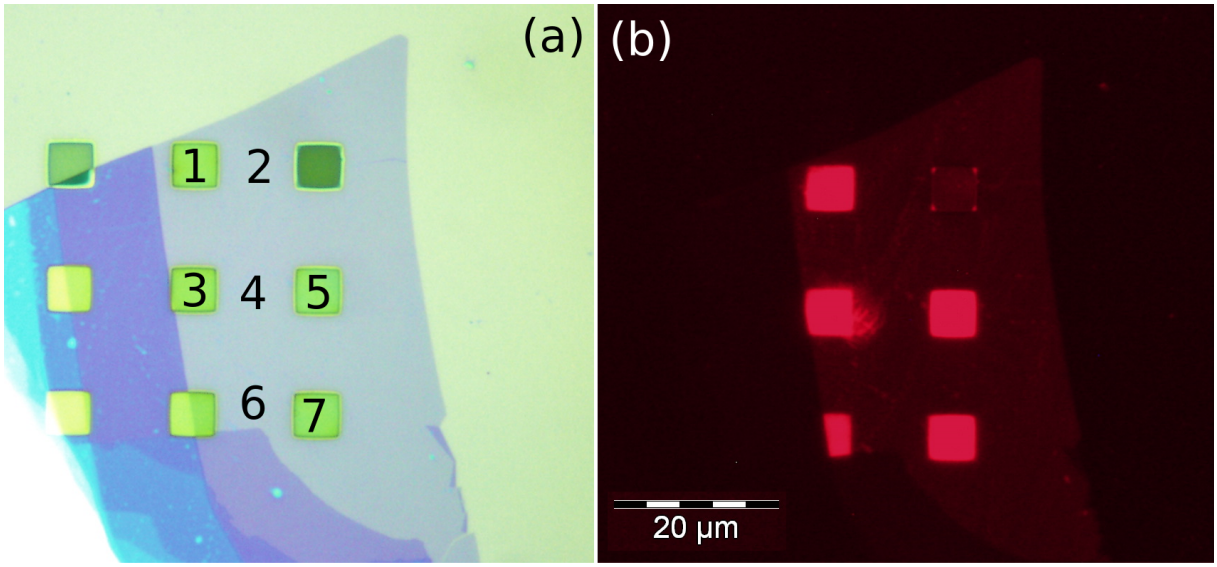

Figure 4.1 – (a) Optical and (b) fluorescence images of the suspended and supported monolayers of MoS_2. Odd numbers represent points were the spectra were taken for suspended monolayers, while even numbers are the points for measurements in the supported ones.

The Raman spectra were measured in all temperatures with a 1 mW laser ($\lambda = 568$ nm) power for all the seven points and the collected data was used as an indication that they were indeed monolayers. We measured the distance between the two well known modes, E^1_{2g} and A_{1g}, and we obtained values between 19-20 cm^{-1} for all suspended and supported points, which are in perfect agreement with values found on the literature [55, 76, 77].

Figure 4.2 shows the Raman spectra collected for points (1) and (2) addressed in Figure 4.1a, at 7 K. The spectra for the other suspended and supported points is very similar. As we raised the temperature, we noticed a wobbling behaviour of the E^1_{2g} and A_{1g} modes around their expected frequency values ($\sim$385 cm^{-1} for E^1_{2g} and $\sim$405 cm^{-1} for A_{1g}). This behaviour could be due to a misconfiguration in the calibration of our

spectrometer, but it may also be due to the fact that the suspended sample is under stress, due to the air trapped beneath it, as explained above. This behaviour will be studied in a future work.

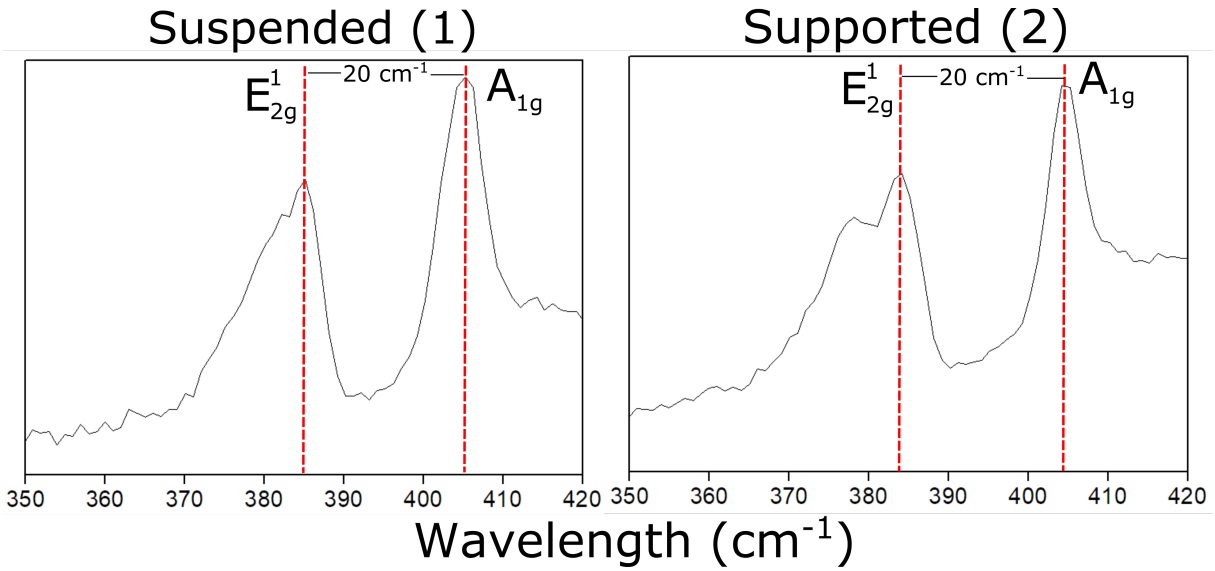

Figure 4.2 – Raman spectra of suspended and supported points of a MoS_2 monolayer at 7 K.

In the PL measurements, the collected spectra were taken with four different laser powers: 400 µW, 600 µW, 800 µW and 1 mW. For the 600 µW and 1 mW powers, we collected data for all the points in 21 different temperatures within the temperature range mentioned above. For the other two laser powers, only five temperatures in this range were considered in the measurements: 7 K, 55 K, 105 K, 200 K and 300 K. The spectra for all the supported points were very similar, so we chose one of them [point (6)] to exemplify the features of the supported monolayer. The same applied for the suspended ones, and in this case, we chose point (1) to account for the suspended monolayer behaviour.

All the PL spectra were fitted using a combination of Gaussians and split Voigts (which is a convolution of a Gaussian and a Lorentzian), with a different number of fitted curves between the suspended and the supported monolayers. We tried to understand the behaviour of each peak with temperature and laser power to properly identify their origin. The detailed study of these spectra is given in the sections below.

4.1 Supported Monolayer

The evolution of the photoluminescence spectrum, for the supported monolayer, as the temperature increases and for two different excitation powers, is shown in Figure 4.3. The spectra were normalized in respect to the high energy feature at around 1.9 eV.

For both powers, the spectra evolve similarly with the change in temperature and we can see that the difference in intensity between the two main features is higher for the lower excitation power. The high energy peak redshifts and becomes the main feature in the spectrum as the low energy peak rapidly falls off with the increase in temperature.

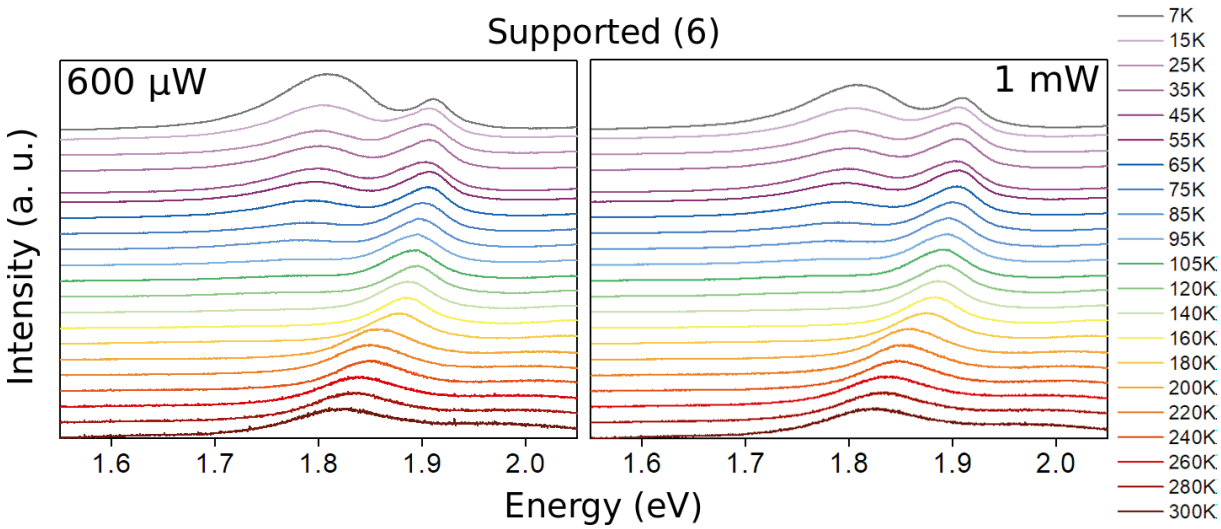

Figure 4.3 – Photoluminescence spectra for one of the supported MoS_2 monolayer for two different excitation powers and within a temperature range of 7 K to 300 K.

We use the 600 µW excitation power spectra to continue our description of the supported MoS_2 monolayer features. We fitted five curves to adjust the experimental data in all temperatures measured: three Gaussians and two split Voigts. Figure 4.4 shows the experimental data and the corresponding fitting curves for some of the temperatures considered. Very narrow features appear at the high-energy end of the spectra and those become more evident as the temperature increases. These sharp peaks are the Raman modes, visible in the spectra due to the excitation wavelength being close to the exciton B energy.

In Figure 4.3 and Figure 4.4 we see a long tail at the low energy end of the spectra, and we found that the best fitting for that part was achieved using a splitVoigt and a Gaussian curve. We decided to label these curves L2 and L1, respectively. Excitons A and B photoluminescence are easily fitted with a Gaussian curve each, but the same does not occur for the trion peak. Instead, we found that a better fitting was achieved using another split Voigt for this feature. The split Voigt introduces an asymmetry in the trion energy and this was also seen by Christopher et al. [78] in a temperature-dependent photoluminescence study of MoS_2 monolayers. This behaviour is understood as the ejection of one electron (or hole) with considerable momentum and the following recombination of the remaining electron-hole pair.

Similar photoluminescence spectra for MoS_2 monolayers were seen by Tongay et

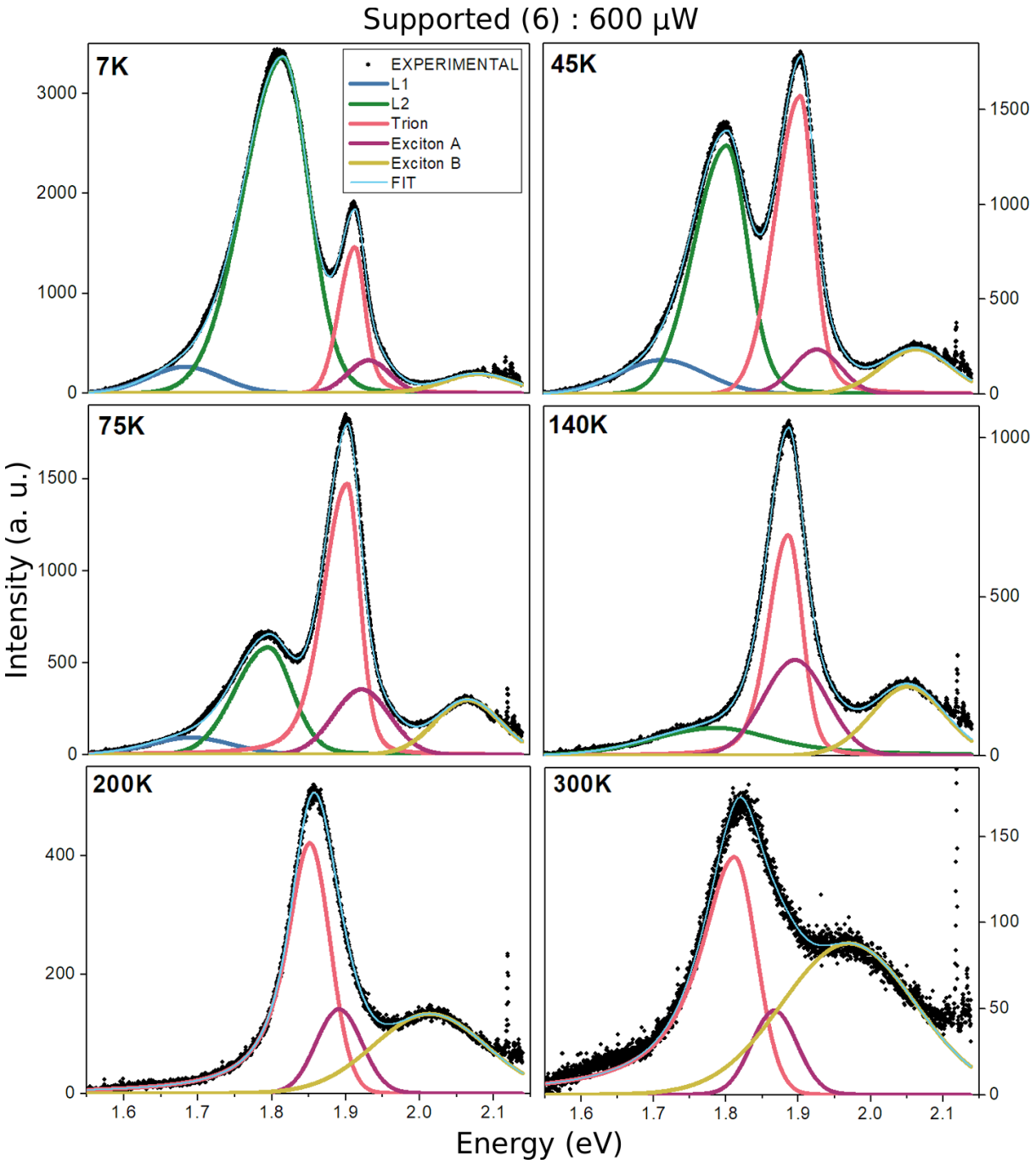

Figure 4.4 – Fitted curves for the PL spectra of a supported MoS_2 monolayer with 600 µW laser power for some of the temperatures measured. The black dots are the experimental data and the coloured lines are the fitting curves. The dark blue line (L1), purple (exciton A) and yellow (exciton B) are Gaussians, while the green (L2) and red (trion) are split Voigts.

al. [20], Korn et al. [76], Jadczak et al. [79] and Pandey and Soni [48]. They all see a similar evolution of the PL spectrum with increasing temperature, where the low-energy shoulder quenches as the temperature is increased. This feature is usually attributed to defects and bound excitons, but biexcitonic recombinations were also considered by Pandey and Soni [48].

Figure 4.5 shows the change in energy of all identified emission peaks of the supported sample, for two different excitation powers. All other supported samples show similar behaviour. As the temperature increases, we see a redshift for all peaks. For all semiconductors, the bandgap decreases as the temperature rises. Qualitatively, this can be explained by the increase of the inter atomic spacing with increased thermal energy. The exciton recombination is expected to follow the decrease in energy of the bandgap, since the exciton is formed by the interaction between an electron in the conduction band and a hole in the valence band, as explained before. The exciton binding energy can also depend on the temperature, but on a smaller degree, so in general one would expect the excitonic recombination to follow the redshift of the bandgap as the temperature is increased.

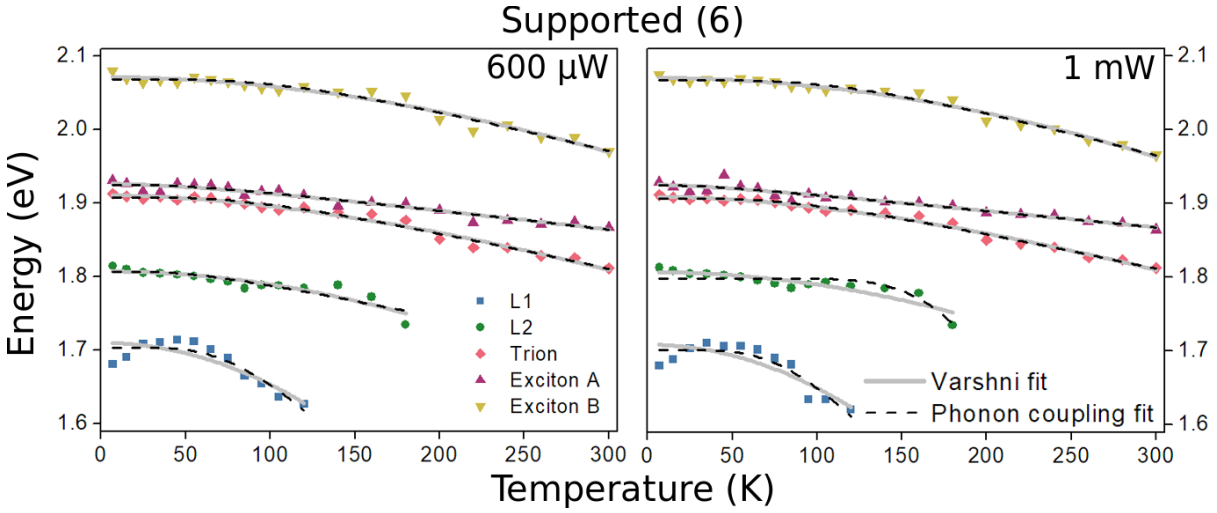

Figure 4.5 – Energy shift as a function of temperature of all identified peaks on the supported monolayer for 600 µW (left) and 1 mW (right) excitation powers. Coloured points are the original data L1 (blue squares), L2 (green circles), trion (red diamonds) and excitons A (purple pointed-up triangles) and B (yellow pointed-down triangles). The curves are the two types of fittings we tried: Varshni (grey full-line) and Phonon coupling (black dashed-line).

The change in temperature of a semiconductor bandgap is difficult to model theoretically. Usually, the dependency of gap energy with temperature is represented by the well known semi-empirical Varshni equation [80]:

$$E_g(T) = E_0 - \frac{\alpha T^2}{T + \beta} \tag{4.1}$$

where E_0 is the bandgap energy at 0 K and α and β are fitting parameters typical of each material. In general, β is loosely associated with the Debye temperature, so for MoS_2 it should be of the order of 250 K. The grey full-line curves in Figure 4.5 are fits to the energy change with temperature using the Varshni formula. The parameters for the fits are shown in Table 1.

The fitting parameters in the Varshni formula are difficult to interpret and to relate to known physical quantities. Motivated by this, O'Donnel and Chen [81] proposed another

Table 1 – Varshni law parameters for each feature in the supported monolayer fitting.

	$\mathbf{E_0}$ (eV)		α (eV K^{-1})		β (K)	
	600 µW	1 mW	600 µW	1 mW	600 µW	1 mW
L1	1.71	1.71	$4.16 \cdot 10^{11}$	$8.37 \cdot 10^{18}$	$7.32 \cdot 10^{16}$	$1.42 \cdot 10^{24}$
L2	1.81	1.81	911	1370	$5.11 \cdot 10^{18}$	$8.12 \cdot 10^{8}$
Trion	1.91	1.91	$9.68 \cdot 10^{-4}$	$9.44 \cdot 10^{-4}$	561	555
Exciton A	1.93	1.93	$2.84 \cdot 10^{-4}$	$2.35 \cdot 10^{-4}$	110	63.9
Exciton B	2.07	2.07	$2.73 \cdot 10^{-3}$	12.8	2110	$1.07 \cdot 10^{7}$

empirical expression to replace Varshni's:

$$E_g(T) = E_0 - SE_P\left(coth\left(\frac{E_P}{2k_BT}\right) - 1\right) \tag{4.2}$$

where E_0 is again the gap at zero Kelvin, E_P is an average phonon energy for the material and S is a dimensionless coupling constant. The black dashed lines in Figure 4.5 are fits for the data using this expression. The parameters used for the fits are shown in Table 2.

Table 2 – O'Donnel's law parameters for each feature in the supported monolayer fitting.

	$\mathbf{E_0}$ (eV)		**S**		$\mathbf{E_P}$ (meV)	
	600 µW	1 mW	600 µW	1 mW	600 µW	1 mW
L1	1.70	1.70	4.69	5.96	88.1	98.2
L2	1.81	1.80	0.786	51.7	51.2	357
Trion	1.91	1.91	0.852	0.824	85.1	82.9
Exciton A	1.92	1.92	0.426	0.362	48.8	31.1
Exciton B	2.07	2.07	0.993	1.12	101	120

It is clear that both expressions provide very similar fits. Looking at the parameters provided by the fitting of Equation 4.2, one sees an average phonon in the 30 meV to approximatelly 100 meV, which is reasonable, since the A_{1g} and E^1_{2g} phonons of MoS_2 are around 50 meV. The exception is peak L2, at excitation power 1 mW, which has fitting parameter $E_P \sim 360$ meV, a too high phonon energy. It also displays an extremely high coupling constant S, of the order of 50. The other coupling constants have acceptable values, around 1.

Looking at the Varshni fits for the same curves, we see that only for peaks identified as exciton A and trion the temperature β is of the order of hundreds of Kelvins, which is reasonable.

We also plotted the intensity change of each feature as a function of temperature. These are shown in Figure 4.6 for two different excitation powers. The intensity axis is in a logarithmic scale, and we can see the almost linear decay of both L1 and L2 peaks as the

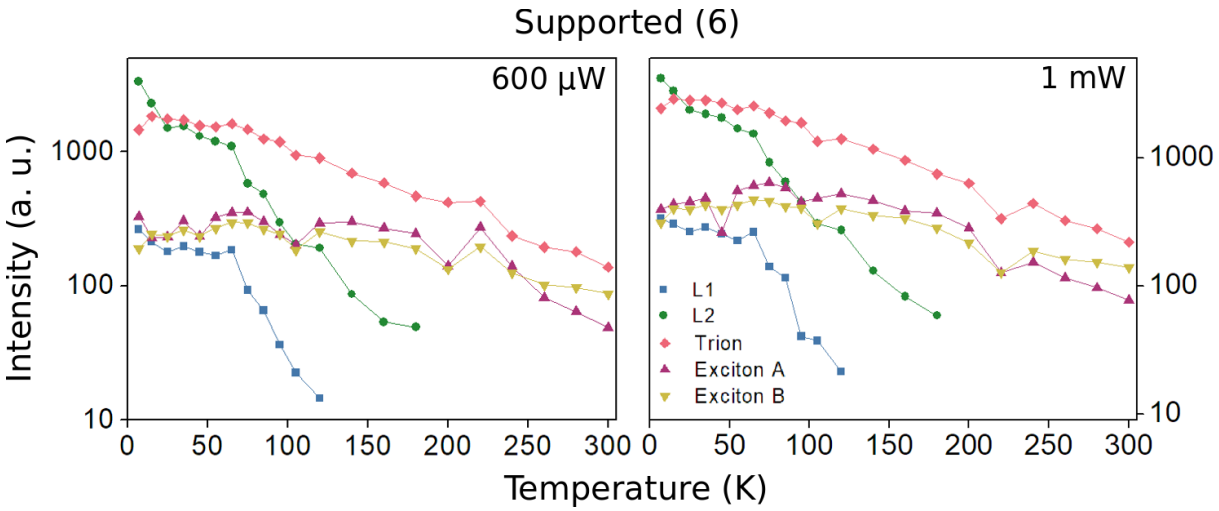

Figure 4.6 – Evolution of the intensity for the supported monolayer as a function of temperature, for 600 µW (left) and 1 mW (right) excitation powers. Each color is attributed to one feature of the fitted spectrum: blue squares for L1, green circles for L2, red diamonds for trion, purple pointed-up-triangles for exciton A and yellow pointed-dow-triangles for exciton B.

temperature increases. This behaviour is typical for bound excitons, and we expect that their intensity is related to their binding energy as expressed in the following equation:

$$I = Ce^{\frac{-E_l}{k_B T}} \tag{4.3}$$

where C is a constant, T the temperature and E_l the exciton binding energy. We can take the logarithm of each side in equation 4.3, which gives:

$$ln(I) = ln(C) + \frac{-E_l}{k_B}\frac{1}{T} \tag{4.4}$$

Figure 4.7 shows a graph of $ln(I)$ versus T^{-1} for the L1 and L2 peaks and the fit of Equation 4.4 to the experimental data, for both excitation powers considered above. We compute E_l multiplying the slopes of the fitted curves by k_B. The obtained parameters and corresponding binding energies found are shown in Table 3.

Table 3 – Binding energies for the L1 and L2 features in the supported monolayer.

	Slope (K)		$\mathbf{E_l}$ (meV)	
	600 µW	1 mW	600 µW	1 mW
L1	266.9	259.6	23.0	22.3
L2	320.5	372.2	27.6	32.1

Our fitting returned the binding energies of around 23 meV for the L1 feature, while the L2 feature presented higher values, closer to 30 meV. These are consistent with bound excitons binding energies.

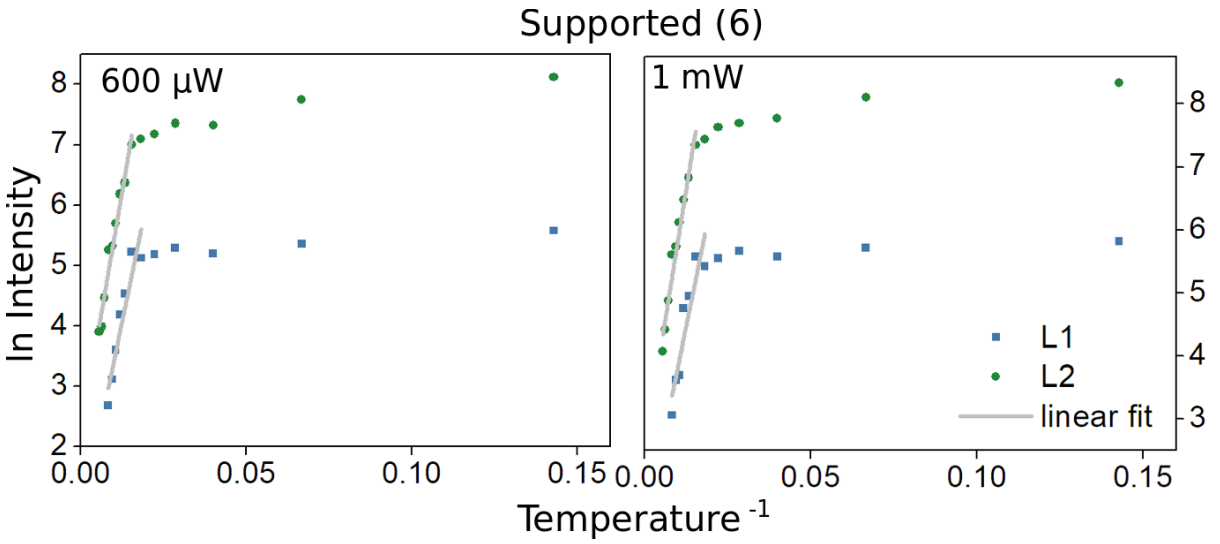

Figure 4.7 – Logarithm of the intensity as a function of the inverse of temperature for the L1 (blue squares) and L2 (green circles) features in the supported monolayer, for 600 µW (left) and 1 mW (right) excitation powers. The grey line shows the linear fit for obtaining the binding energies of these bound excitons.

To make sure that our fitting accurately reproduce the quasi-particles in the system, we fitted these same curves for the other excitation power spectra. Although there were only few temperatures to consider for 400 µW and 800 µW, they showed how each peak changed with the increase in laser power. This is particularly important to correctly identify the features in our fittings.

The luminescence intensity I in the PL spectrum is related to the incident laser power P by a power relation:

$$I = CP^n \tag{4.5}$$

where C is a constant and n the power index. Taking the logarithmic of this equation yields:

$$ln(I) = A + nln(P) \tag{4.6}$$

which is a linear equation, with $A = ln(C)$ and n the slope. This linear relation is very important in the identification of excitons, trions, biexcitons and bound states. Figure 4.8 shows the linear fit of equation 4.6 for all the features identified in the supported monolayer.

For bound excitons, the behaviour should be sublinear, as is observed in Figure 4.8. Both excitons should have a power dependency of $n = 1$, which is found to be very close in our fitting. On the other hand, the expected power dependecy for the trion should be n between 1 and 2, and this is not found in our study, although its dependency still higher then the excitonic ones. For biexcitons, the slope should be close to $n = 2$.

We see that our fit gives a reasonable explanation for the behaviour of the supported monolayer as the temperature changes. From the analysis of emission energies with

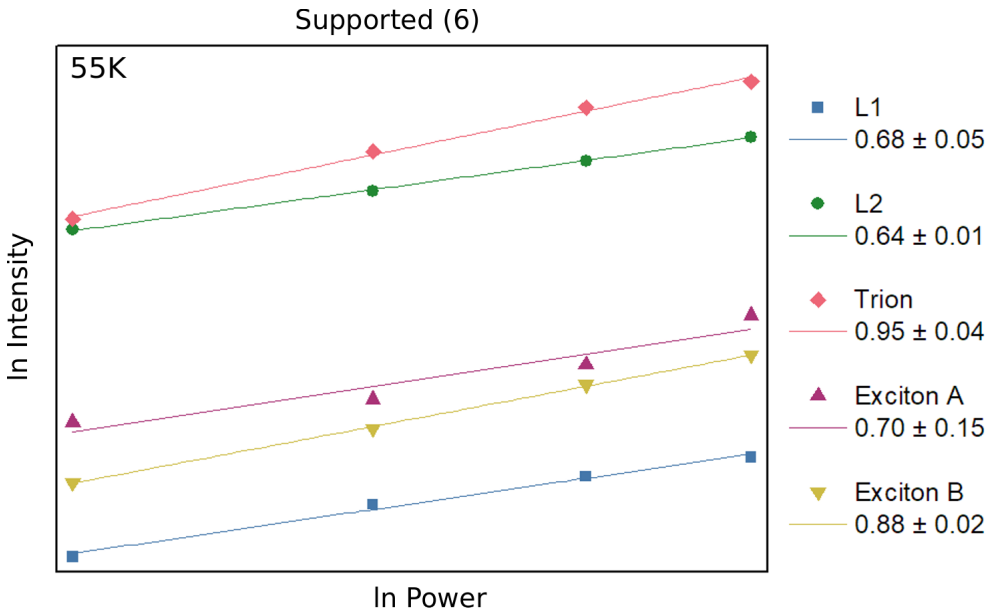

Figure 4.8 – Linear fit (coloured lines) for the logarithmic of intensity versus logarithmic of laser power at 55 K. The values at the far-right indicate the slope (n) for each fitting . L1 (blue squares) and L2 (green circles) show sublinear behaviour. Trion (red diamonds), exciton A (purple pointed-up triangles) and exciton B (yellow pointed-down triangles) all show sublinear behaviour, although very close to n=1.

temperature, we obtain a confirmation of the identification of the exciton A and trion peaks, although their intensity-power relation does not show the linear (for the neutral excitons) and supra-linear (trion) behaviour. This could be due to the difficult associated in fitting many curves into the experimental data. We conclude also that there are additonal phenomena affecting the energy change of the other peaks, as the temperature is varied. For the peak identified as exciton B, we propose the hypothesis that this peak is actually a convolution of the emission of the exciton B and an excited state of the exciton A, as first suggested by Pandey and Soni [48]. For peaks L1 and L2 we propose that their origin is excitons bound to defects in the material, one of them possibly sulphur vacancies and the other one to be identified. In this way, the change in temperature of these emissions will also depend on the binding energies of the excitons and the emission energy should not follow the gap closely. This is further confirmed by computing their respective binding energies and showing their sublinear behaviour for the intensity-power relation. Further work, with the support of theoretical calculations is needed to clarify these points.

4.2 Suspended Monolayer

Figure 4.9 shows how the PL spectra of one of the suspended monolayer changes with the increase in temperature for 600 µW and 1 mW laser powers. The other suspended samples show almost identical behaviour. Similarly to the supported monolayer, there is

a broad low-energy peak (at ∼1.8 eV) and this is much more intense in the suspended than it is in the supported monolayer. Again, with the increase in temperature, this feature redshifts and fades quickly. The high energy peak (at ∼1.9 eV) also redshifts with temperature.

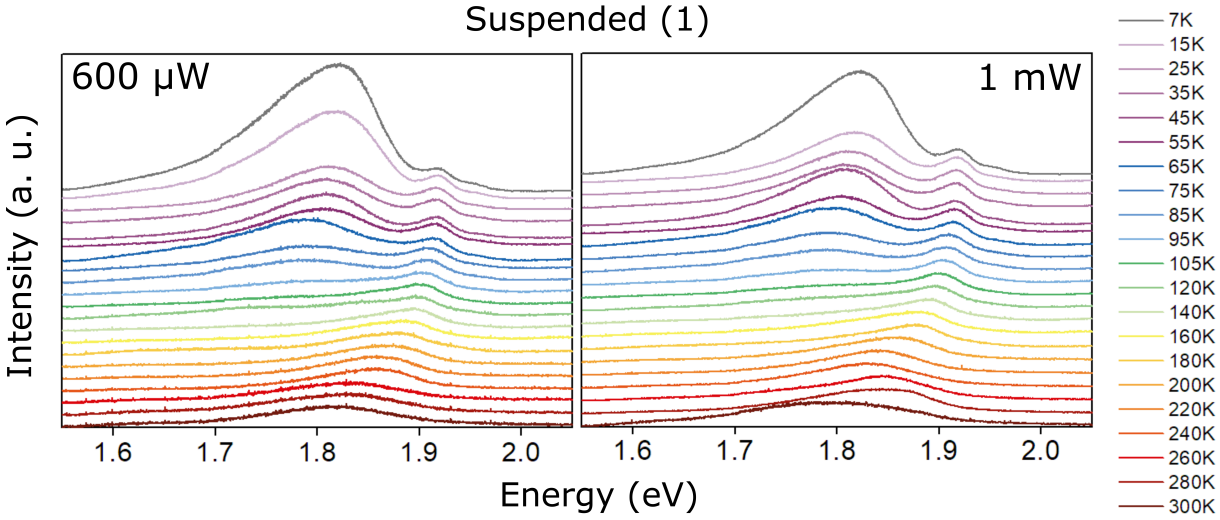

Figure 4.9 – Photoluminescence spectra for one of the suspended MoS_2 monolayers for two different excitation powers and within a temperature range of 7 K to 300 K.

As for the supported monolayer, we chose to use the spectra under 600 µW excitation power to detail our description of the features of the PL of the suspended one. Instead of fitting five curves, as in the previous case, we found it impossible to have an accurate fitting without at least six curves. So we maintained the three Gaussians and two split Voigts and their respective labels (L1, L2, trion, excitons A and B) and decided to add another Gaussian between L2 and the trion, which we called L3. Figure 4.10 shows the experimental data and these fitting curves, for some of the temperatures considered. At 120 K is clear that there is at least 4 peaks below 1.9 eV.

We use the same argumentations for the fittings of the Gaussians and split Voigts as we used in the supported monolayer. The new feature (L3) could be as well adjusted with a split Voigt or a Gaussian, and we decided to go with the last for simplicity.

As with the supported monolayer, the low-energy shoulder in the suspended one decreases in intensity with the increase of temperature, but it does not fade out as in the previous case. The L1 and L2 features lose their importance very rapidly, but remain present even at room temperature. The L3 feature, on the other hand, loses importance for the trion feature, but is still very intense at high temperatures.

Figure 4.11 shows the change in energy of all identified emission for one of the suspended samples, for two different excitation powers. The other suspended samples show similar behaviour. Again, the grey full-lines are Varshni fits to the data and the black dotted-lines are fits using O'Donnel and Chen's equation. The fitting parameters for

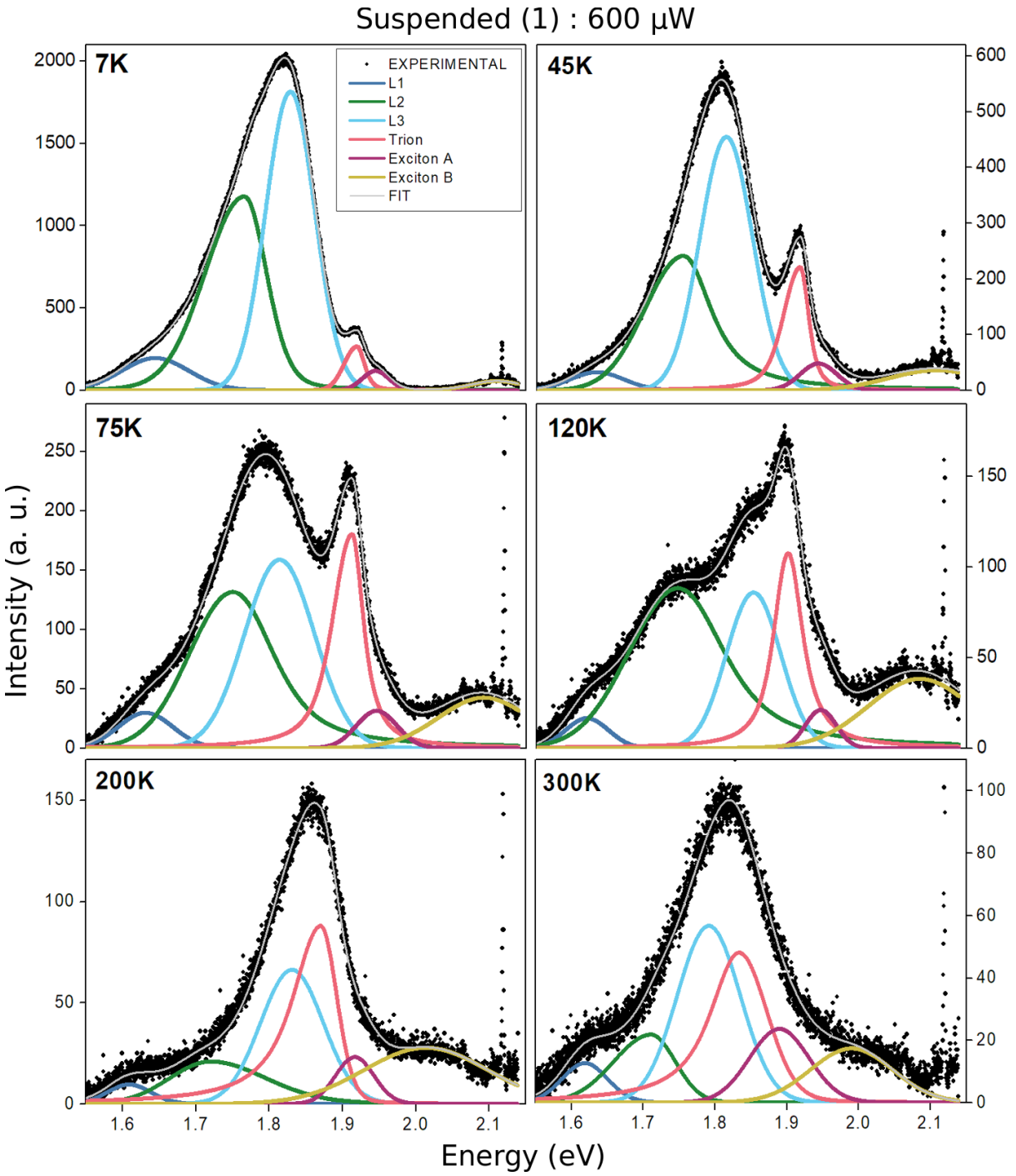

Figure 4.10 – Fitted curves for the PL spectra of a suspended MoS_2 monolayer with 600 μW laser power for some of the temperatures measured. The black dots are the experimental data and the coloured lines are the fitting curves. The dark blue line (L1), light blue (L3), purple (exciton A) and yellow (exciton B) are Gaussians, while the green (L2) and red (trion) are split Voigts.

Varshni's are shown in Table 4, while the phonon-coupling parameters are shown in Table 5. Again, we obtain reasonable fitting parameters for the exciton A and trion emissions, with average phonon energy E_P in the range 35 meV to 100 meV and coupling constants somewhat below unit. The Varshni parameters for these peaks are also acceptable, with

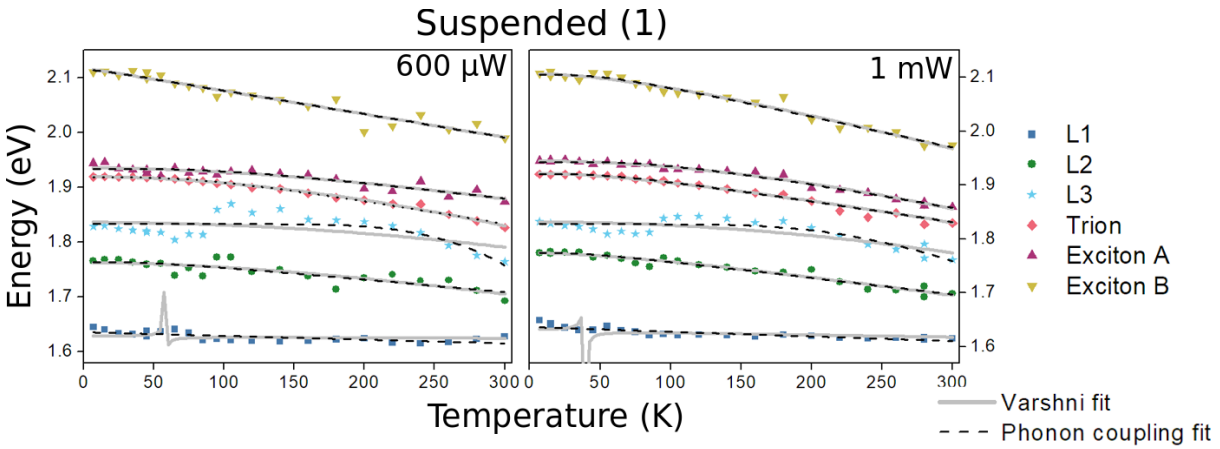

Figure 4.11 – Energy shift as a function of temperature of all identified peaks on the suspendedd monolayer for 600 µW (left) and 1 mW (right) excitation powers. Coloured points are the original data L1 (dark-blue squares), L2 (green circles), L3 (light-blue stars), trion (red diamonds) and excitons A (purple pointed-up triangles) and B (yellow pointed-down triangles). The curves are the two types of fittings we tried: Varshni (grey full-line) and Phonon coupling (black dashed-line).

β temperatures of the order of some hundreds of Kelvins. The surprise is that the peak at 1.76 eV (L2) at low temperatures, which is only seen in the suspended samples, also produces reasonable fitting parameters, with phonon energies of 35-50 meV. This seems to suggest that this is a well-behaved exciton, probably bound to a defect as well, but which follows closely the bandgap. We propose that this defect could be an oxygen linked to a sulphur vacancy, but this hypothesis needs further experimental and theoretical confirmation. Also, it should be noted that for the highest excitation power, 1 mW, the peak identified as exciton B displays reasonable fitting parameters. This might indicate that, at this high excitation power, the emission around 2.1 eV is dominated possibly by the excited state of exciton A, as proposed by Pandey and Soni [48].

Table 4 – Varshni law parameters for each feature in the suspended monolayer fitting.

	$\mathbf{E_0}$ (eV)		α (eV K^{-1})		β (K)	
	600 µW	1 mW	600 µW	1 mW	600 µW	1 mW
L1	1.63	1.63	$1.10 \cdot 10^{-5}$	$4.20 \cdot 10^{-5}$	−57.8	−39.2
L2	1.76	1.77	$5.10 \cdot 10^{-4}$	$3.77 \cdot 10^{-4}$	504	132
L3	1.84	1.83	$5.60 \cdot 10^{8}$	$-9.03 \cdot 10^{15}$	$1.11 \cdot 10^{15}$	−1.41
Trion	1.92	1.92	$1.34 \cdot 10^{-3}$	$4.78 \cdot 10^{-4}$	1050	170
Exciton A	1.94	1.94	$6.36 \cdot 10^{-4}$	$1.42 \cdot 10^{-3}$	715	1130
Exciton B	2.12	2.11	$4.25 \cdot 10^{-4}$	$7.30 \cdot 10^{-4}$	6.65	173

We have plotted the intensity change of each feature as a function of temperature as well. These are shown in Figure 4.12 for two different excitation powers. We see that the L3 intensity changes differently from the other bound states, L1 and L2. It begins

Table 5 – O'Donnel's law parameters for each feature in the suspended monolayer fitting.

	$\mathbf{E_0}$ (eV)		**S**		$\mathbf{E_P}$ (meV)	
	600 µW	1 mW	600 µW	1 mW	600 µW	1 mW
L1	1.64	1.64	0.110	0.140	$-5.51 \cdot 10^{-4}$	$-6.38 \cdot 10^{-4}$
L2	1.76	1.77	0.379	0.503	47.0	36.0
L3	1.83	1.83	21.2	3.59	531	333
Trion	1.92	1.92	0.722	0.647	80.4	54.2
Exciton A	1.93	1.94	0.512	0.779	97.6	92.1
Exciton B	2.12	2.11	0.688	0.947	−8.26	47.7

close to L2 until around 140 K and then decreases almost the same as the trion.

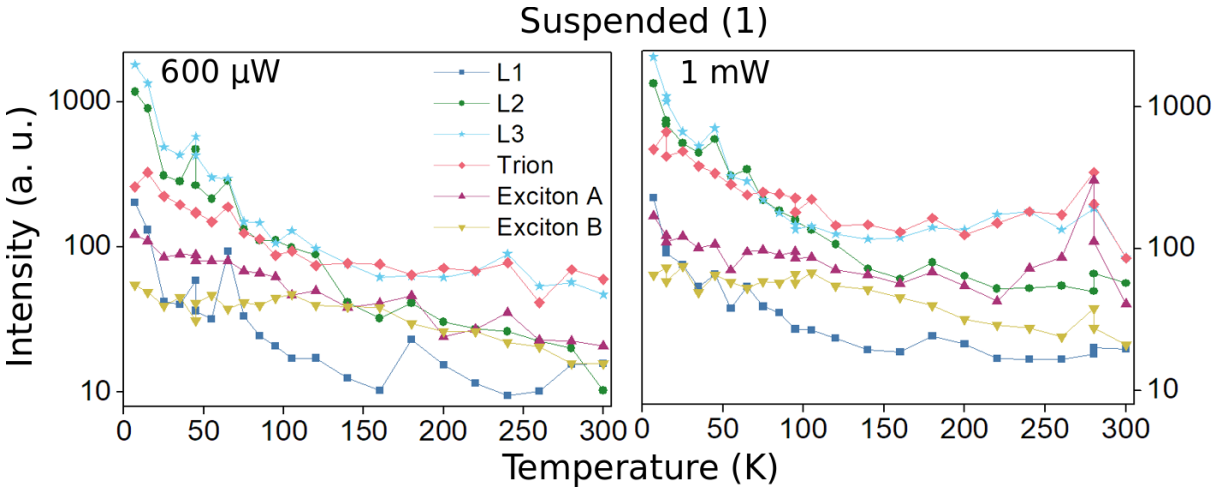

Figure 4.12 – Evolution of the intensity for the suspended monolayer as a function of temperature, for 600 µW (left) and 1 mW (right) excitation powers. Each colour is attributed to one feature of the fitted spectrum: dark-blue squares for L1, green circles for L2, light-blue stars for L3, red diamonds for trion, purple pointed-up-triangles for exciton A and yellow pointed-dow-triangles for exciton B.

As we have done for the bound excitons L1 and L2 in the supported monolayer, we took the logarithm of the intensity of the bound excitons in the suspended monolayer as a function of the inverse of the temperature. This is shown in Figure 4.13. We used a linear fit, as indicated by the gray lines in Figure 4.13, to get information on the binding energy E_l of these excitons. The obtained parameters and respective binding energies are shown in Table 6.

We see that the binding energies acquired by this method for the suspend monolayer are much lower than the values obtained for the supported samples, being below 20 meV. This could be due to the difficulty in adjusting many curves into the experimental data, but it is an indication that the binding energies of the excitons to the defects for the suspended layer are smaller than the binding energies in the supported sample. One possible explanation for this is the strain in the suspended layer, due to the trapped air

beneath the membrane.

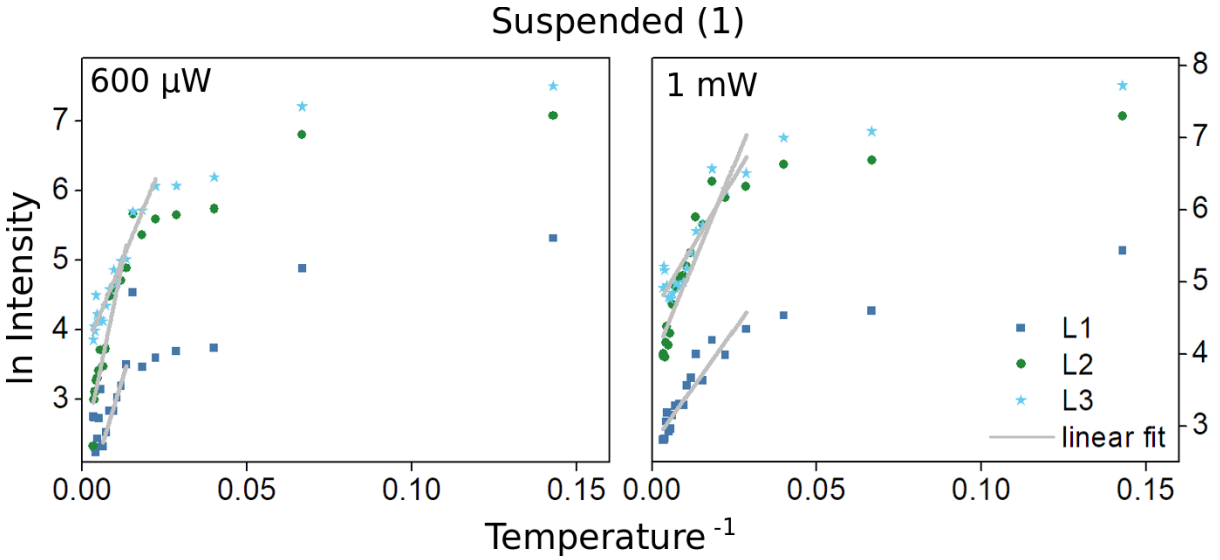

Figure 4.13 – Logarithm of the intensity as a function of the inverse of temperature for the L1 (dark-blue squares), L2 (green circles) and L1 (light-blue stars) features in the suspended monolayer, for 600 µW (left) and 1 mW (right) excitation powers. The grey line shows the linear fit for obtaining the binding energies of these bound excitons.

Table 6 – Binding energies for the L1 and L2 features in the suspended monolayer.

	Slope (K)		$\mathbf{E_l}$ (meV)	
	600 µW	1 mW	600 µW	1 mW
L1	154.3	64.01	13.3	5.52
L2	226.1	110.3	19.5	9.50
L3	115.0	75.7	9.91	6.52

Our final approach to understand the nature of these features in the suspended monolayer was to plot the power-intensity relation and calculate the power relation between them, as done for the supported monolayer. We plotted the logarithm of intensity as a function of the logarithm of the excitation power at 55 K for all the features in the suspended monolayer, as shown in Figure 4.14. The values obtained for L1 and L2 agree well with those found in the supported monolayer, with an inclination below unity. The trion and exciton B features also present reasonable values, with slopes close to one, and so does exciton A, in spite of a somewhat odd behaviour, with a a power dependency that does not clearly follow the $I = CP^n$ behaviour. The unknown feature L3 show sublinear behaviour, but very close to unity, which is unusual for a bound exciton.

In conclusion, we see that the model used in fitting the suspended MoS_2 monolayer data is not as good as the one chosen for the supported monolayer. Some refinements need

to be done and there is strong indication that we need to take into account the effects caused by the strain in the suspended monolayer.

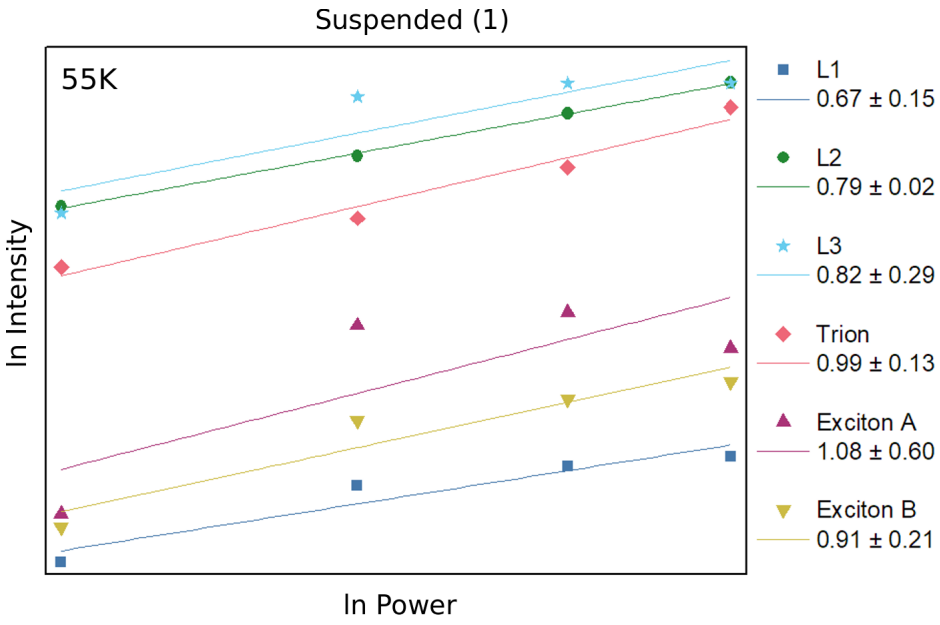

Figure 4.14 – Linear fit (coloured lines) for the logarithmic of intensity versus logarithmic of laser power at 55 K. The values at the far-right indicate the slope (n) for each fitting . L1 (dark-blue squares) and L2 (green circles) show sublinear behaviour. L3 (light-blue stars), trion (red diamonds) and exciton B (yellow pointed-down triangles) all show sublinear behaviour, although very close to n=1. Exciton A shows a slope around unity, but the data is not a good fit to a straight line, with a high error, 1.0 ± 0.6.

5 Conclusions and Future Work

In this work we studied the optical properties of suspended and supported monolayers of MoS_2. We created a matrix of holes on SiO_2/Si substrate and transferred a MoS_2 monolayer on top of it, effectively covering some of the holes. Spectra of a set of suspended and supported points within this sample were taken, in a range of different temperatures and excitation powers. At the low energy end of the spectra, two distinctive features are noticed: an asymmetric energy tail, specially in the suspended monolayer, and a broad prominent peak around 1.80 eV that fades at high temperatures, vanishingly completely for the supported monolayer. We fitted a combination of Gaussian curves and split Voigts to try and account for this behaviour. The number of fitted curves is different for each type: a total of 5 curves for the supported monolayer and 6 for the suspended one. We ascribed these curves to the known neutral excitons, A and B, a trion and bound excitons. We plotted the intensity change and energy shift with temperature for each curve, and tried to ascribe to each a power law for the intensity and excitation power relation. This provides support for our model for the quasi-particles present in the system (excitons, trion, bound excitons) but also gives evidence that further work is needed to clarify the role of the strain in the suspended layers and the nature of the defects to which the excitons are bound.

Our next goal then is to refine our fitting model, perhaps adding another curve to account for the broadening of the high-energy part of the spectrum, which is possible due to the excited state of the neutral exciton A. We also want to understand the part that biexcitons, reported for similar samples by other authors, and bound states take in the photoluminescence spectra, and how they evolve with the increase in temperature. Also, to our knowledge, a complete study of the optical properties of the suspended monolayer (not only for MoS_2 but also for other types of TMDs, such as WS_2) is lacking, and this opens up possibilities to explore new physics in these materials.

Bibliography

[1] B. Radisavljevic, A. Radenovic, J. Brivio, V. Giacometti, and A. Kis, "Single-layer MoS_2 transistors," *Nature Nanotechnology*, vol. 6, pp. 147–150, 2011.

[2] J. Lee, Z. Wang, K. He, J. Shan, and P. X. L. Feng, "High frequency MoS_2 nanomechanical resonators," *ACS Nano*, vol. 7, pp. 6086–6091, 2013.

[3] F. H. L. Koppens, T. Mueller, P. Avouris, A. C. Ferrari, M. S. Vitiello, and M. Polini, "Photodetectors based on graphene, other two-dimensional materials and hybrid systems," *Nature Nanotechnology*, vol. 9, pp. 780–793, 2014.

[4] D. Jariwala, V. K. Sangwan, L. J. Lauhon, T. J. Marks, and M. C. Hersam, "Emerging device applications for semiconducting two-dimensional transition metal dichalcogenides.," *ACS Nano*, vol. 8, pp. 1102–1120, 2014.

[5] F. Xia, H. Wang, D. Xiao, M. Dubey, and A. Ramasubramaniam, "Two-dimensional material nanophotonics," *Nature Photonics*, vol. 8, pp. 899–907, 2014.

[6] N. Zibouche, A. Kuc, J. Musfeld, and T. Heine, "Transition-metal dichalcogenides for spintronic applications," *Annalen der Physik*, vol. 526, No. 9-10, p. 395–401, 2014.

[7] D. Lembke, S. Bertolazzi, and A. Kis, "Single-layer MoS_2 electronics," *Accounts of Chemical Research*, vol. 48, pp. 100–110, 2015.

[8] Y. Ye, Z. J. Wong, X. Lu, X. Ni, H. Zhu, X. Chen, Y. Wang, and X. Zhang, "Monolayer excitonic laser," *Nature Photonics*, vol. 9, pp. 733–737, 2015.

[9] K. F. Mak and J. Shan, "Photonics and optoelectronics of 2D semiconductor transition metal dichalcogenides," *Nature Photonics*, vol. 10, pp. 216–226, 2016.

[10] K. F. Mak, C. Lee, J. Hone, J. Shan, and T. F. Heinz, "Atomically thin MoS_2: A new direct-gap semiconductor," *Physical Review Letters*, vol. 105, p. 136805, 2010.

[11] A. Splendiani, L. Sun, Y. Zhang, T. Li, J. Kim, C. Y. Chim, G. Gally, and F. Wang, "Emerging photoluminescence in monolayer MoS_2," *Nano Letters*, vol. 10, pp. 1271–1275, 2010.

[12] A. K. Geim and I. V. Grigorieva, "Van der Waals heterostructures," *Nature*, vol. 499, pp. 419–425, 2013.

[13] Y. Sun, R. Wang, and K. Liu, "Substrate induced changes in atomically thin 2-dimensional semiconductors: Fundamentals, engineering, and applications," *Applied Physics Reviews*, vol. 4, p. 011301, 2017.

[14] Q. H. Wang, K. Kalantar-Zadeh, A. Kis, J. N. Coleman, and M. S. Strano, "Electronics and optoelectronics of two-dimensional transition metal dichalcogenides," *Nature Nanotechnology*, vol. 7, pp. 699–712, 2012.

[15] R. Ganatra and Q. Zhang, "Few-layer MoS_2: A promising layered semiconductor," *ACS Nano*, vol. 8(5), pp. 4074–4099, 2014.

[16] S. Z. Butler, S. M. Hollen, L. Cao, Y. Cui, J. A. Gupta, H. R. Gutiérrez, T. F. Heinz, S. S. Hong, J. Huang, A. F. Ismach, E. Johnston-Halperin, M. Kuno, V. V. Plashnitsa, R. D. Robinson, R. S. Ruoff, S. Salahuddin, J. Shan, L. Shi, M. G. Spencer, M. Terrones, W. Windl, and J. E. Goldberger, "Progress, challenges, and opportunities in two-dimensional materials beyond graphene," *ACS Nano*, vol. 7, pp. 2898–2926, 2013.

[17] M. Chhowalla, H. S. Shin, G. Eda, L. J. Li, K. P. Loh, and H. Zhang, "The chemistry of two-dimensional layered transition metal dichalcogenide nanosheets," *Nature Chemistry*, vol. 5, pp. 263–275, 2013.

[18] D. Sercombe, S. Schwarz, O. D. Pozo-Zamudio, F. Liu, B. J. Robinson, E. A. Chekhovich, I. I. Tartakovskii, O. Kolosov, and A. I. Tartakovskii, "Optical investigation of the natural electron doping in thin MoS_2 films deposited on dielectric substrates," *Scientific Reports*, vol. 3, p. 3489, 2013.

[19] H. Shi, R. Yan, S. Bertolazzi, J. Brivio, B. Gao, A. Kis, D. Jena, H. G. Xing, and L. Huang, "Exciton dynamics in suspended monolayer and few-layer MoS_2 2D crystals," *ACS Nano*, vol. 7, pp. 1072–1080, 2013.

[20] S. Tongay, J. Suh, C. Ataca, W. Fan, A. Luce, J. S. Kang, J. Liu, C. Ko, R. Raghunathanan, J. Zhou, F. Ogletree, J. Li, J. C. Grossman, and J. Wu, "Defects activated photoluminescence in two-dimensional semiconductors: interplay between bound, charged, and free excitons," *Scientific Reports*, vol. 3, p. 2657, 2013.

[21] P. Tonndorf, R. Schmidt, P. Böttger, X. Zhang, J. Börner, A. Liebig, M. Albrecht, C. Kloc, O. Gordan, D. R. T. Zhang, S. M. de Vasconcellos, and R. Bratschitsch, "Photoluminescence emission and Raman response of monolayer MoS_2, $MoSe_2$ and WSe_2," *Optics Express*, vol. 21, no. 4, 2013.

[22] N. Scheuschner, O. Ochedowski, A. M. Kaulitz, R. Gillen, M. Schleberger, and J. Maultzsch, "Photoluminescence of freestanding single- and few-layer MoS_2," *Physical Review B*, vol. 89, p. 125406, 2014.

[23] J. A. Wilson and A. D. Yoffe, "The transition metal dichalcogenides discussion and interpretation of the observed optical, electrical and structural properties," *Advances in Physics*, vol. 18, pp. 193–335, 1969.

[24] R. R. R. López, "Optical properties of transition metal dichalcogenides on GaAs," masther's thesis, Universidade Federal de Minas Gerais, 2018.

[25] N. Ashcroft and D. Mermin, *Solid State Physics*. Cengage Learning, 1976.

[26] Z. Y. Zhu, Y. C. Cheng, and U. Schwingenschlögl, "Giant spin-orbit-induced spin splitting in two-dimensional transition-metal dichalcogenide semiconductors," *Physical Review B*, vol. 84, p. 153402, 2011.

[27] C. Kittel, *Introduction to Solid State Physics*. LTC, 2006.

[28] W. Kohn, "Nobel Lecture: Electronic structure of matter-wave functions and density functionals," *Reviews of Modern Physics*, vol. 71, pp. 1253–1266, 1999.

[29] H. Shi, H. Pan, Y. W. Zhang, and B. I. Yakobson, "Quasiparticle band structures and optical properties of strained monolayer MoS_2 and WS_2," *Physical Review B*, vol. 87, p. 155304, 2013.

[30] E. Cappelluti, R. Roldán, J. A. Silva-Guillén, P. Ordejón, and F. Guinea, "Tight-binding model and direct-gap/indirect-gap transition in single-layer and multilayer MoS_2," *Physical Review B*, vol. 88, p. 075409, 2013.

[31] G. B. Liu, W. Y. Shan, Y. Yao, W. Yao, and D. Xiao, "Three-band tight-binding model for monolayers of group-vib transition metal dichalcogenides," *Physical Review B*, vol. 88, p. 085433, 2013.

[32] E. Ridolfi, D. Le, T. S. Rahman, E. R. Mucciolo, and C. H. Lewenkopf, "A tight-binding model for MoS_2 monolayers," *Journal of Physics Condensed Matter*, vol. 27, p. 365501, 2015.

[33] A. Kormányos, G. Burkard, M. Gmitra, J. Fabian, V. Zólyomi, N. D. Drummond, and V. Fal'ko, "$\mathbf{k} \cdot \mathbf{p}$ theory for two-dimensional transition metal dichalcogenide semiconductors," *2D Materials*, vol. 2, p. 022001, 2015.

[34] S. Aas and C. Bulutay, "Strain dependence of photoluminescence and circular dichroism in transition metal dichalcogenides: a $\mathbf{k} \cdot \mathbf{p}$ analysis," *Optics Express*, vol. 26, pp. 28672–28681, 2018.

[35] A. Kuc, N. Zibouche, and T. Heine, "Influence of quantum confinement on the electronic structure of the transition metal sulfide TS_2," *Physical Review B*, vol. 83, p. 245213, 2011.

[36] D. Xiao, G. B. Liu, W. Feng, X. Xu, and W. Yao, "Coupled spin and valley physics in monolayers of MoS_2 and other group-vi dichalcogenides," *Physical Review Letters*, vol. 108, p. 196802, 2012.

[37] K. Kośmider, J. W. González, and J. Fernández-Rossier, "Large spin splitting in the conduction band of transition metal dichalcogenide monolayers," *Physical Review B*, vol. 88, p. 245436, 2013.

[38] X. Xu, W. Yao, D. Xiao, and T. F. Heinz, "Spin and pseudospins in transition metal dichalcogenides," *Nature Physics*, vol. 10, pp. 343–350, 2014.

[39] T. Cao, G. Wang, W. Han, H. Ye, C. Zhu, J. Shi, Q. Niu, P. Tan, E. Wang, B. Liu, and J. Feng, "Valley-selective circular dichroism of monolayer molybdenum disulphide," *Nature Communications*, vol. 3:887, pp. 1–5, 2012.

[40] H. Zeng, J. Dai, W. Yao, D. Xiao, and X. Cui, "Valley polarization in MoS_2 monolayers by optical pumping," *Nature Nanotechnology*, vol. 7, pp. 490–493, 2012.

[41] M. Fox, *Optical Properties of Solids*. Oxford University Press, 2010.

[42] A. Ramasubramaniam, "Large excitonic effects in monolayers of molybdenum and tungsten dichalcogenides," *Physical Review B*, vol. 86, p. 115409, 2012.

[43] A. Chernikov, T. C. Berkelbach, H. M. Hill, A. Rigosi, Y. Li, O. B. Aslan, D. R. Reichman, M. S. Hybertsen, and T. F. Heinz, "Exciton binding energy and nonhydrogenic Rydberg series in monolayer WS_2," *Physical Review Letters*, vol. 113, p. 076802, 2014.

[44] K. F. Mak, K. He, C. Lee, G. H. Lee, J. Hone, T. F. Heinz, and J. Shan, "Tightly bound trions in monolayer MoS_2," *Nature Materials*, vol. 12, pp. 207–211, 2013.

[45] M. Currie, A. T. Hanbicki, G. Kioseoglou, and B. T. Jonker, "Optical control of charged exciton states in tungsten disulfide," *Applied Physics Letters*, vol. 106, p. 201907, 2015.

[46] Y. You, X. X. Zhang, T. C. Berkelbach, M. S. Hybertsen, D. R. Reichman, and T. F. Heinz, "Observation of biexcitons in monolayer WSe_2," *Nature Physics*, vol. 11, pp. 477–482, 2015.

[47] I. Paradisanos, S. Germanis, N. T. Pelekanos, C. Fotakis, E. Kymakis, G. Kioseoglou, and E. Stratakis, "Room temperature observation of biexcitons in exfoliated WS_2 monolayers," *Applied Physics Letters*, vol. 110, p. 193102, 2017.

[48] J. Pandey and A. Soni, "Unraveling biexciton and excitonic excited states from defect bound states in monolayer MoS_2," *Applied Surface Science*, vol. 463, pp. 52–57, 2019.

[49] G. Plenchinger, P. Nagler, J. Kraus, N. Paradiso, C. Strunk, C. Schüler, and T. Korn, "Identification of excitons, trions and biexcitons in single-layer WS_2," *Physica Status Solid*, vol. 9(8), p. 457–461, 2015.

[50] P. Tonndorf, R. Schmidt, R. Schneider, J. Kern, M. Buscema, G. A. Steele, A. Castellanos-Gomez, H. S. J. van der Zant, S. M. de Vasconcellos, and R. Bratschitsch, "Single-photon emission from localized excitons in an atomically thin semiconductor," *Optica*, vol. 2, pp. 347–352, 2015.

[51] A. Castellanos-Gomez, N. Agraït, and G. Rubio-Bollinger, "Optical identification of atomically thin dichalcogenide crystals," *Applied Physics Letters*, vol. 96, pp. 94–97, 2010.

[52] C. Ataca, M. Topsakal, E. Aktürk, and S. Ciraci, "A comparative study of lattice dynamics of three- and two-dimensional MoS_2," vol. 115, p. 16354–16361, 2011.

[53] Q. Yue, J. Kang, Z. Shao, X. Zhang, S. Chang, G. Wang, S. Quin, and J. Li, "Mechanical and electronic properties of monolayer MoS_2 under elastic strain," *Physics Letters A*, vol. 376, pp. 1166–1170, 2012.

[54] S. Bertolazzi, J. Brivio, and A. Kis, "Stretching and breaking of ultrathin MoS_2," *ACS Nano*, vol. 5, pp. 9703–9709, 2011.

[55] C. Lee, H. Yan, L. E. Brus, T. F. Heinz, J. Hone, and S. Ryu, "Anomalous lattice vibrations of single- and few-layer MoS_2," *ACS Nano*, vol. 4, pp. 2695–2700, 2010.

[56] W. H. Chae, J. D. Cain, E. D. Hanson, A. A. Murthy, and V. P. Dravid, "Substrate-induced strain and charge doping in CVD-grown monolayer MoS_2," *Applied Physics Letters*, vol. 111, p. 143106, 2017.

[57] J. D. Hernandez, "Generation of quantum dots via nanoindentation in MoS_2," masther's thesis, Universidade Federal de Minas Gerais, 2016.

[58] A. Castellanos-Gomez, R. Roldán, E. Cappelluti, M. Buscema, F. Guinea, H. S. J. van der Zant, and G. A. Steele, "Local strain engineering in atomically thin MoS_2," *Nano Letters*, vol. 13, pp. 5361–5366, 2013.

[59] H. J. Conley, B. Wang, J. I. Ziegler, R. F. Haglund Jr., S. T. Pantelides, and K. I. Bolotin, "Bandgap engineering of strained monolayer and bilayer MoS_2," *Nano Letters*, vol. 13, pp. 3626–3630, 2013.

[60] K. He, C. Poole, K. F. Mak, and J. Shan, "Experimental demonstration of continuous electronic structure tuning via strain in atomically thin MoS_2," *Nano Letters*, vol. 13, pp. 2931–2936, 2013.

[61] C. R. Zhu, G. Wang, B. L. Liu, X. Marie, X. F. Qiao, X. Zhang, X. X. Wu, H. Fan, P. H. Tan, T. Amand, and B. Urbaszek, "Strain tuning of optical emission energy and polarization in monolayer and bilayer MoS_2," *Physical Review B*, vol. 12, p. 121301, 2013.

[62] C. Rice, R. J. Young, R. Zan, U. Bangert, D. Wolverson, T. Georgiou, R. Jalil, and K. S. Novoselov, "Raman-scattering measurements and first-principles calculations of strain-induced phonon shifts in monolayer MoS_2," *Physical Review B*, vol. 87, p. 081307, 2013.

[63] D. Lloyd, X. Liu, J. W. Christopher, L. Cantley, A. Wadehra, B. L. Kim, B. B. Goldberg, A. K. Swan, and J. S. Bunch, "Band gap engineering with ultralarge biaxial strains in suspended monolayer MoS_2," *Nano Letters*, vol. 16, pp. 5836–5841, 2016.

[64] J. Chaste, A. Missaoui, S. Huang, H. Henck, Z. B. Aziza, L. Ferlazzo, C. Naylor, A. Balan, A. T. C. Johnson Jr., R. Braive, and A. Ouerghi, "Intrinsic properties of suspended MoS_2 on SiO_2/Si pillar arrays for nanomechanics and optics," *ACS Nano*, vol. 12, pp. 3235–3242, 2018.

[65] E. Scalise, M. Houssa, G. Pourtois, V. Afanas'ev, and A. Stesmans, "Strain-induced semiconductor to metal transition in the two-dimensional honeycomb structure of MoS_2," *Nano Research*, vol. 5, pp. 43–48, 2012.

[66] M. Buscema, G. A. Steele, H. S. J. van der Zant, and A. Castellanos-Gomez, "The effect of the substrate on the Raman and photoluminescence emission of single-layer MoS_2," *Nano Research*, vol. 7(4), pp. 561–571, 2014.

[67] Y. Yu, Y. Yu, C. Xu, Y. Q. Cai, L. Su, Y. Zhang, Y. W. Zhang, K. Gundogdu, and L. Cao, "Engineering substrate interactions for high luminescence efficiency of transition-metal dichalcogenides monolayers," *Advanced Functional Materials*, vol. 26, pp. 4733–4739, 2016.

[68] Y. Shi, H. Li, and L. J. Li, "Recent advances in controlled synthesis of two-dimensional transition metal dichalcogenides via vapour deposition techniques," *Chemical Society Reviews*, vol. 44, pp. 2744–2756, 2015.

[69] M. Bosi, "Growth and synthesis of mono and few-layers transition metal dichalcogenides by vapour techniques: a review," *RSC Advances*, vol. 5, p. 75500, 2015.

[70] D. Dumcenco, D. Ovchinnikov, K. Marinov, P. Lazić, M. Gilbertini, N. Marzari, O. L. Sanchez, Y. C. Kung, D. Krasnozhon, M. W. Chen, S. Bertolazzi, P. Gillet, A. F. Morral, A. Radenovic, and A. Kis, "Large-area epitaxial monolayer MoS_2," *ACS Nano*, vol. 4, p. 4611–4620, 2015.

[71] K. S. Novoselov, A. K. Geim, S. V. Morozov, D. Jiang, Y. Zhang, S. V. Dubonos, I. V. Grigorieva, and A. A. Firsov, "Electric field in atomically thin carbon films," *Science*, vol. 306, pp. 666–669, 2004.

[72] M. Yi and Z. Shen, "A review on mechanical exfoliation for the scalable production of graphene," *Journal of Materials Chemistry A*, vol. 3, p. 11700, 2015.

[73] A. Castellanos-Gomez, M. Buscema, R. Molenaar, V. Singh, L. Janssen, H. S. J. van der Zant, and G. A. Steele, "Deterministic transfer of two-dimensional material by all-dry viscoelastic stamping," *2D Materials*, vol. 1(1), 2014.

[74] N. G. Boddeti, S. P. Koenig, R. Long, J. Xiao, J. S. Bunch, and M. L. Dunn, "Mechanics of adhered, pressurized graphene blisters," *Journal of Applied Mechanics*, vol. 80, p. 040909, 2013.

[75] G. Binnig, C. F. Quate, and C. Gerber, "Atomic force microscopy," *Physical Review Letters*, vol. 56, pp. 930–934, 1986.

[76] T. Korn, S. Heydrich, M. Hirmer, J. Schmutzler, and C. Schüller, "Low-temperature photocarrier dynamics in monolayer MoS_2," *Applied Physics Letters*, vol. 99, p. 102109, 2011.

[77] A. Castellanos-Gomez, M. Barkelid, A. M. Goossens, V. E. Calado, H. S. J. van der Zant, and G. A. Steele, "Laser-thinning of MoS_2: On demand generation of a single-layer semiconductor," *Nano Letters*, vol. 12, pp. 3187–3192, 2012.

[78] J. W. Christopher, B. B. Goldberg, and A. K. Swan, "Long tailed trions in monolayer MoS_2: Temperature dependent asymmetry and resulting red-shift of trion photoluminescence spectra," *Scientific Reports*, vol. 7, p. 14062, 2017.

[79] J. Jadczak, J. Kutrowska-Girzycka, P. Kapuściński, Y. S. Huang, A. Wójs, and L. Bryja, "Probing of free and localized excitons and trions in atomically thin WSe_2, WS_2, $MoSe_2$ and MoS_2 in photoluminescence and reflectivity experiments," *Nanotechnology*, vol. 28, p. 395702, 2017.

[80] Y. P. Varshni, "Temperature dependence of the energy gap in semiconductors," *Physica*, vol. 34, pp. 149–154, 1967.

[81] K. P. O'Donell and X. Chen, "Temperature dependence of semiconductor band gaps," *Applied Physics Letters*, vol. 58, pp. 2924–2926, 1991.